*J. Fluid Mech.* (1998), *vol.* 355, *pp.* 193–227. Printed in the United Kingdom



# On linear and nonlinear instability of the incompressible swept attachment-line boundary layer

By VASSILIOS THEOFILIS

DLR, Institute for Fluid Mechanics, Division Transition and Turbulence, Bunsenstraße 10, D-37073 Göttingen, Germany

(Received 8 November 1993 and in revised form 19 March 1997)

The stability of an incompressible swept attachment-line boundary layer flow is studied numerically, within the Görtler–Hämmerlin framework, in both the linear and nonlinear two-dimensional regimes in a self-consistent manner. The initial-boundary-value problem resulting from substitution of small-amplitude excitation into the incompressible Navier–Stokes equations and linearization about the generalized Hiemenz profile is solved. A comprehensive comparison of all linear approaches utilized to date is presented and it is demonstrated that the linear initial-boundary-value problem formulation delivers results in excellent agreement with those obtained by solution of either the temporal or the spatial linear stability theory eigenvalue problem for both zero suction and a layer in which blowing is applied. In the latter boundary layer recent experiments have documented the growth of instability waves with frequencies in a range encompassed by that of the unstable Görtler–Hämmerlin linear modes found in our simulations. In order to enable further comparisons with experiment and, thus, assess the validity of the Görtler–Hämmerlin theoretical model, we make available the spatial structure of the eigenfunctions at maximum growth conditions.

The condition on smallness of the imposed excitation is subsequently relaxed and the resulting nonlinear initial-boundary-value problem is solved. Extensive numerical experimentation has been performed which has verified theoretical predictions on the way in which the solution is expected to bifurcate from the linear neutral loop. However, it is demonstrated that the two-dimensional model equations considered do not deliver subcritical instability of this flow; this strengthens the conjecture that three-dimensionality is, at least partly, responsible for the observed discrepancy between the linear theory critical Reynolds number and the subcritical turbulence observed either experimentally or in three-dimensional numerical simulations. Further, the present nonlinear computations demonstrate that the unstable flow has its line of maximum amplification in the neighbourhood of the experimentally observed instability waves, in a manner analogous to the Blasius boundary layer. In line with previous eigenvalue problem and direct simulation work, suction is observed to be a powerful stabilization mechanism for naturally occurring instabilities of small amplitude.

## 1. Introduction

An attachment line is formed on the windward surface of any cylindrical object immersed in fluid flow at an angle, as schematically depicted in figure 1. At Reynolds numbers typically encountered in flows of technological importance laminar flow

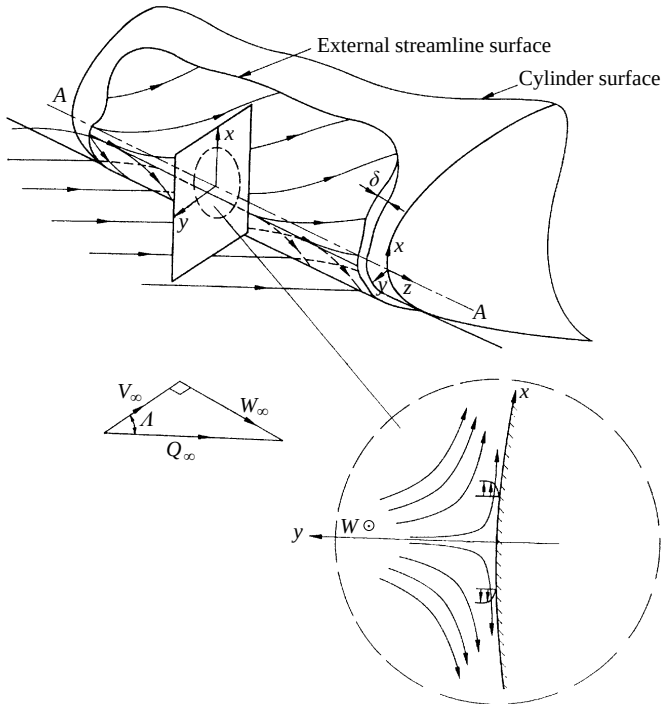


FIGURE 1. Schematic representation of leading edge boundary layer flow.

in the boundary layer formed in the vicinity of such an attachment line has been observed to support instability waves, akin to the Tollmien–Schlichting waves found in the classical Blasius flow. The growth in space, or time, of these instability waves can lead to transition and turbulence. It is clear that turbulence originating in the attachment-line boundary layer will propagate into the flow away from the plane defined by the attachment line and the wall normal. This feeding of the boundary layer off the attachment line, with turbulent flow originating at the attachment line itself, renders ineffective any of the classical means of laminar flow control which focus on crossflow instability away from the attachment line. It was indeed puzzling for the investigators of pioneering swept wing configurations that, although measures had been taken to control the powerful, inviscid in nature, crossflow instability, laminar flow over swept wings could not be maintained (Lippisch 1976 and references therein; Horten & Selinger 1983 and references therein; Gray 1952).

Our understanding of incompressible swept attachment-line boundary layer (hereafter also referred to as leading-edge boundary layer, LEBL) instability has advanced somewhat since the early days (Reed, Saric & Arnal 1996). Significant contributions were made by the experimental investigations at the National Physical Laboratory and the College of Aeronautics in Europe and at Northrop in the United States. Gaster (1967) summarized the former; he was the first to appreciate that one of the ways for turbulent flow to enter the attachment-line boundary layer on a swept wing is through the wing–body junction. Gaster suggested the use of a device, placed in the wing-root area, which would locally decelerate the part of the flow which was about to enter the attachment-line boundary layer (Gaster 1965). If originally turbulent, the flow would undergo reverse transition and the boundary layer in the attachment line itself would (potentially) thus be kept in a laminar state. Pfenninger & Bacon

(1969), on the other hand, were the first to detect the existence of naturally occurring sinusoidal instability waves in the attachment-line boundary layer formed on the windward surface of a 45° swept cylinder. These investigators went on to document, to the benefit of later theoretical work, the conditions of maximum spatial growth of these waves.

The early experimental work was revisited by Poll (1979) whose experiments paved the way for the theoretical developments that followed. It was first established that attachment line and crossflow are two distinct instability mechanisms, viscous and inviscid, respectively, in nature. The latter is operative off the attachment line, at locations where the relative direction of the inviscid and the limiting streamlines supports a (small) three-dimensional component in the basic flow (Poll 1985). This crossflow results in the total basic flow profile acquiring an inflection point which gives rise to a powerful inviscid instability mechanism, the signature of which is the well-known crossflow vortices (Gregory, Stuart & Walker 1955; Reed & Saric 1989). Instability waves naturally occurring at the attachment line itself, on the other hand, were found to occur largely at the conditions that the earlier investigators had suggested. The conditions for their existence were documented and compiled into engineering criteria for the determination of the state, laminar or turbulent, of the LEBL under given conditions. The results of Poll were corroborated through and supplemented by the experiments performed in parallel at ONERA/CERT by Arnal and co-workers (Arnal, Coustols & Jullien 1984; Arnal 1993).

Linear instability, along the classic lines developed by Tollmien and Schlichting for the Blasius boundary layer, was considered responsible for the waves observed in the swept attachment-line boundary layer. Based on the analogies between the (streamwise) Blasius flow and the component of the LEBL basic flow along the leading edge, Poll (1979) used the latter as input to the Orr–Sommerfeld (OS) equation, neglecting the essential three-dimensionality of the LEBL basic flow profile. This mathematical inconsistency resulted in asymptotic agreement between experimental results and numerical solutions to the OS equation being obtained only at the limit of increasingly large Reynolds number. The question of a linear critical Reynolds number could thus not be addressed. Hall, Malik & Poll (1984) derived and solved a formally consistent system of linear stability equations for the flow under consideration. They incorporated the Görtler–Hämmerlin (GH) assumption for the small-amplitude perturbation velocities (Görtler 1955; Hämmerlin 1955) and pointed out that there is no rational means of reduction of the resulting LEBL linear stability system to the OS equation. Hall *et al.* proceeded to solve the temporal eigenvalue problem, calculating a linear critical Reynolds number that compared better than that corresponding to solution of the OS equation with experimental results obtained under conditions favouring growth of small-amplitude perturbations. Monitoring the analogies in the spectra of the OS equation (Grosch & Salwen 1978) and the LEBL system Theofilis (1995) has recently demonstrated analytically the observed asymptotic agreement between the results of the OS equation applied to the attachment-line boundary layer (Poll 1979) and the large Reynolds number limit of the LEBL system of Hall *et al.* (1984).

Floryan & Dallmann (1990) used linear theory incorporating the GH assumption in their receptivity analysis of LEBL flow with distributed surface roughness. They demonstrated that roughness generates steady streamwise vorticity, but the roughness itself may be eliminated by the surface stresses generated if surface erosion or wall flexibility is admitted. Further, Floryan & Dallmann showed that large thermal stresses generated by the concentration of heat flow at the tips of the roughness along

the leading edge may cause structural damage to the leading edge surface itself. This work concentrated on a small neighbourhood of the attachment line and the first term in a series expansion which describes streamwise-varying roughness in the vicinity of the attachment line.

Linear instability is by no means the only route to transition to turbulence in attachment-line boundary layer flow. While the aforementioned combined theoretical and experimental efforts have established a linear critical Reynolds number $Re \approx 583$, sustained turbulence in LEBL flow has been documented experimentally at Reynolds numbers as low as $Re \approx 235$ (Poll 1979). Instead of attributing the residual discrepancies between experimental results and the Hall *et al.* theory regarding the critical Reynolds number to unquantifiable by-pass mechanisms (Morkovin & Reshotko 1989), Hall & Malik (1986) applied weakly nonlinear analysis along the lines of the Stuart–Watson theory (Stuart 1960; Watson 1960) to study the behaviour of LEBL flow past the stage of linear instability. Their theory predicted that this flow may be destabilized at a subcritical Reynolds number by finite-amplitude disturbances; numerical solutions to the initial-boundary value problem indeed yielded a critical value of $Re \approx 535$. A first step towards bridging the gap between experimental observations and theoretical predictions was thus provided.

Hall & Seddougui (1990) analysed the interaction of oblique waves with the unstable linear two-dimensional modes of the LEBL system using triple-deck theory (see e.g. Duck & Burggraf 1986) and monitoring both the linear and the weakly nonlinear regimes of perturbation. Hall & Seddougui demonstrated that in the immediate vicinity of the attachment line both low-frequency oblique modes and modes whose frequency is comparable to that of the unstable two-dimensional wave may cause breakdown of LEBL flow. The discussion of these oblique modes was only possible at the high Reynolds number limit in order for the analytical tools utilized to be applicable. It is, nevertheless, clear that the three-dimensional instability discovered has the potential to destroy the two-dimensional nonlinear equilibrium solutions of Hall & Malik.

Numerical simulations of LEBL flow started in the mid 1980s and have played an increasingly important role in shaping our understanding of the instability mechanisms involved. Spalart (1988) presented the first direct numerical simulation (DNS) results of three-dimensional LEBL flow. A number of significant results of this work merit discussion. Most importantly, Spalart's work did not use *a priori* the GH assumption. At conditions that permitted linear growth, according to the earlier theories, Spalart demonstrated, to within numerical tolerance, that the linear perturbations indeed assumed the form that Görtler and Hämmerlin had proposed "for reasons of mathematical convenience". From a numerical point of view Spalart's DNS results were obtained by imposing what is now described as a buffer-domain approach in the (chordwise) direction of strong acceleration of the flow. In so doing the flow was permitted to develop off the attachment-line vortical structures reminiscent of those observed experimentally. The homogeneous spanwise direction, along the attachment line, was taken to be periodic. Further, the three-dimensionality of the full system of equations considered permitted breakdown to turbulence which could be maintained at $Re \approx 260$. A suggestion of this observation is that the search for subcriticality in the present flow should move away from linear mechanisms. Starting from a turbulent flow field Spalart was able to demonstrate relaminarization of the flow by lowering the Reynolds number or by applying suction. The unswept limit of LEBL flow was found to be linearly and nonlinearly stable, in line with the analytical prediction of Wilson & Gladwell (1978). In a number of three-dimensional runs performed,

however, Spalart (1988) found no evidence of the nonlinear equilibrium solutions that the two-dimensional model equations considered by Hall & Malik (1986) were reported to produce.

Jiménez *et al.* (1990) considered numerically the two-dimensional limit of LEBL flow, subject to the GH assumption. Performing numerical experiments they concluded that the two-dimensional flow does not support subcritical solutions. Jiménez *et al.* put forward the suggestion that three-dimensional mechanisms are responsible for the observed subcriticality. The absence of two-dimensional nonlinear equilibria in the simulations of Spalart (1988) may, conceivably, be attributed to the difficulties in comparisons between results delivered by the three-dimensional code of Spalart and those that the two-dimensional GH code of Hall & Malik (1986) yields. The result of Jiménez *et al.* (1990) on subcriticality, however, is in direct contradiction with that of Hall & Malik (1986), who considered the same model equations; the issue of nonlinear subcritical solutions of the two-dimensional model equations has, thus, been left open.

Joslin (1995) studied three-dimensional instabilities in the LEBL region using DNS. In contrast to the work of Spalart (1988) Joslin treated the spanwise direction spatially. In so doing he compared DNS results with spatial linear theory along the attachment line and reported satisfactory agreement being obtained. However, Joslin imposed homogeneous Dirichlet or Neumann boundary conditions on the perturbations in the chordwise direction. He reported that use of these boundary conditions in the direction of flow acceleration, which are inherently restrictive in the form of perturbations that they permit to grow, does not alter the stability results obtained at the attachment line provided that the chordwise extent of the integration domain (resolved by 25 Chebyshev polynomials) is taken to be large enough. Joslin went on to assert that his DNS revealed the nonlinear equilibria predicted by the analysis and computation of the two-dimensional initial-boundary-value problem of Hall & Malik (1986).

Theofilis, Duck & Poll (1989) and Theofilis (1993) demonstrated that formulation of the two-dimensional LEBL flow as an initial-boundary-value problem and linearization about the generalized Hiemenz profile yields results analogous to those delivered by the eigenvalue problem considered by Hall *et al.* (1984); we expand upon this point herein. Further, it was shown that linear disturbances in the two-dimensional LEBL flow respond to suction of the boundary layer in the manner predicted by the eigenvalue problem in Hall *et al.* and also demonstrated in the three-dimensional DNS of Spalart. The neglect of self-interaction of perturbations in Theofilis (1993), however, prohibited addressing the question of subcriticality and the apparently contradictory results in the literature; this is one of the topics on which we focus here.

As already discussed, the magnitude of the discrepancy in the critical Reynolds numbers delivered by linear and weakly nonlinear theory on one hand, and the lowest Reynolds number at which turbulence has been observed in experiments and DNS on the other, suggests that mechanisms beyond those described by linear theory must be studied. It is interesting, in this respect, to define the point of departure of new theoretical efforts, in particular with respect to nonlinearity and three-dimensionality. The present contribution focuses on this question by addressing the nonlinear evolution of linear instability waves which are subject to the GH assumption. Aside from the motivation for a new initial-boundary-value problem study† provided by the apparent

† The terms initial-boundary-value problem and DNS are used interchangeably in the context of the present nonlinear calculations, as are the terms eigenvalue problem and linear stability theory.

inconsistencies in the literature on the issue of subcritical instability and its relation to breakdown to turbulence in LEBL flow, new experimental results (Poll, Danks & Yardley 1996) provide the opportunity to make further assessments of the validity of the GH model as a departure point for future theoretical studies. The assumptions made herein are in line with those made by Hall & Malik (1986) and Jiménez *et al.* (1990); conclusions are based, of necessity, on the results of a large but finite number of numerical experiments performed under a variety of initial conditions.

It should be clear at this point that the only safe conclusions on the existence of nonlinear subcritically growing solutions, based on the results of a finite number of nonlinear runs utilizing arbitrary forms and amplitudes of perturbations, are the affirmative ones. Absence of such solutions, on the other hand, cannot guarantee that they do not exist; it may well happen that the choice of parameters in the runs performed delivers solutions outside the basin of attraction of a potentially existing subcritically unstable solution. A safer approach to identify the latter is to map the nonlinear neutral surface of stable travelling waves; although this procedure, in conjunction with the solution of an eigenvalue problem, is well established in stability analysis (Herbert 1977; Koch 1992) it has only been attempted for the present problem in the DNS of Jiménez *et al.* We further note that a treatment of the stability problem of the present constant-thickness (spanwise) boundary layer using parabolized stability equations (Bertolotti 1991) on the attachment-line plane, is not expected to deliver improved results compared to those that the spatial eigenvalue problem (Theofilis 1995) yields.

The paper is structured as follows. We solve in §2 the eigenvalue problem using a different formulation of the equations to that used for the initial-boundary value problem and an alternative, inherently more accurate numerical treatment to those used in the past, namely spectral (Chebyshev) collocation. Spatial eigenvalue problem and Gaster-transformed temporal eigenvalue problem and initial-boundary-value problem results are compared amongst themselves and with experimentally available results. The temporal eigenvalue problem solution provides us with independently obtained information on the eigenspectrum; this is utilized in the nonlinear computations that follow in §3. Realistic forcing functions are considered and a large integration domain is utilized such that (*a*) a zero perturbation boundary condition may be imposed in the far field and (*b*) at least one subharmonic of the unstable fundamental wavenumber is included in the simulation. Results of relevance to the physical problem are presented and analogies with the Blasius boundary layer are discussed. Concluding remarks are furnished in §4.

## 2. The linear problem revisited

### 2.1. *The generalized Hiemenz boundary layer*

Some introductory presentation of the physical problem is in order at this point. The geometry of the flow under consideration is depicted in figure 1. The assumption is made that the basic flow over the leading edge of an infinite swept cylinder may be treated as locally flat, which stems from the largeness of the free-stream Reynolds number (Goldstein 1938). The oncoming flow $Q_\infty$ outside the boundary layer is taken to be a stagnation-line flow comprising components $(U_\infty, V_\infty, W_\infty)$ in the streamwise (chordwise) $x$, normal $y$ and spanwise $z$ directions respectively; the latter, homogeneous, direction has been treated as periodic. No physical length scale exists in this boundary layer; with the aid of the chordwise component of velocity $U_e$,

evaluated at the boundary layer edge, the local strain rate of the flow $S = (\mathrm{d}U_e/\mathrm{d}x)_{x=0}$ and the viscosity $\nu$, a length scale constructed as $\Delta = (\nu/S)^{1/2}$. Since $U_e$ is taken to depend linearly on $x$ in what follows, $\Delta$ will be defined here as $\Delta = (\nu L/U_e)^{1/2}$, with $L$ an $O(1)$ length. The Reynolds number $Re$ of this constant-thickness boundary layer flow, customarily denoted by $\bar{R}$, is $Re = W_e\Delta/\nu$. The relation $R_\theta \approx 0.404Re$ links the momentum-thickness Reynolds number $R_\theta$ to $Re$, if no suction is applied.

In the absence of any disturbance, the basic flow is taken to be of the form

$$U = S\ x\ \bar{u}(y)\,; \quad V = S\ \Delta\ \bar{v}(y)\,; \quad W = Re\ S\ \Delta\ \bar{w}(y) = W_e\ \bar{w}(y).$$

Substituting this structure into the incompressible Navier–Stokes equations a system of ordinary differential equations results for the determination of the basic-flow velocity vector $(\bar{u}, \bar{v}, \bar{w})$

$$\bar{u} + \bar{v}' = 0, \tag{2.1}$$

$$\bar{v}''' + (\bar{v}')^2 - \bar{v}\ \bar{v}'' - 1 = 0, \tag{2.2}$$

$$\bar{w}'' - \bar{v}\ \bar{w}' = 0, \tag{2.3}$$

subject to the boundary conditions

$$\bar{v}(0) = \kappa; \quad \bar{v}'(0) = 0; \quad \bar{v}'(\infty) = -1,$$

$$\bar{w}(0) = 0; \quad \bar{w}(\infty) = 1.$$

Here a prime denotes differentiation with respect to the LEBL variable $\eta = y/\Delta$ and $\kappa$ is a non-dimensional parameter used to control suction in the boundary layer. This reduced form of the Navier–Stokes equations represents a generalization of the well-known Hiemenz flow (Hiemenz 1911) in that, in addition to the plane stagnation-point flow, it incorporates a non-zero spanwise velocity component. It is well known that stability results are highly sensitive to the accuracy of the basic profile. Two alternative approaches were employed for the calculation of the latter. Equation (2.2) is of the Falkner–Skan class and accurate solutions to this problem may be obtained efficiently by spectral collocation based on Chebyshev polynomials (Streett, Zang & Hussaini 1984). Spectral integration operations (Pruett & Streett 1991) may then be applied to equations (2.1) and (2.3) in order to calculate the streamwise and spanwise basic flow components. Using this approach the need for interpolation between grids in subsequent stability calculations, a potential source of errors creeping in the numerical solution, is eliminated. Alternatively, a straightforward shooting technique may be employed to solve (2.1)–(2.3) in order to obtain the basic flow velocity profile for different values of the suction parameter $\kappa$. If this approach is used the result must be obtained on a large number of nodes in order to minimize the interpolation errors. Both approaches have been used and the numerically obtained results were found to be in excellent agreement with the profiles given, for example, by Rosenhead (1963).

Quantities significant from an engineering point of view, such as shape factor and skin friction of the (zero-suction) generalized Hiemenz flow assume the values $H = 2.54$ and $c_f = 0.461/R_\theta$, as opposed to $H = 2.59$ and $c_f = 0.664/R_\theta$, respectively, for Blasius flow (Arnal 1993). Furthermore, the spanwise velocity profile of the generalized Hiemenz flow resembles closely the streamwise Blasius one. These analogies led to the application of the Orr–Sommerfeld equation in the early theoretical studies of the stability of the LEBL problem. From a mathematical point of view a significant difference between the flat-plate boundary layer and the infinite swept attachment-line

boundary layer is that the basic flow in the former is typically obtained by application of boundary layer theory, namely implicit assumption of large Reynolds number; the basic flow of the incompressible LEBL on the other hand is an exact solution to the Navier–Stokes equations. As a consequence, the stability analysis and the search for an $O(1)$ critical Reynolds number in the latter flow, unlike the former, may be performed in a self-consistent framework.

### 2.2. *The perturbed flow*

For completeness we present next the equations governing the initial-boundary-value problem to be solved. These result from substitution of the decomposition, due to Görtler (1955) and Hämmerlin (1955),

$$u = S\,x\,\{\bar{u} + Re\,\hat{u}\,E\}, \tag{2.4}$$

$$v = W_e\left\{\frac{\bar{v}}{Re} + \hat{v}\,E\right\}, \tag{2.5}$$

$$w = W_e\,\{\bar{w} + \hat{w}\,E\}, \tag{2.6}$$

with $E = \mathrm{e}^{\mathrm{i}(\beta z - \omega t)}$, into the velocity–vorticity form of the Navier–Stokes equations. In the temporal framework considered the real spanwise wavenumber, denoted by $\beta$, and the complex $\omega$ and $c$ are related by the relationship $\omega = \beta c$. Physical significance is attached to the real part of $\omega$ which indicates frequency, while the imaginary part of $\omega$ is the growth rate. The rotational form of the Navier–Stokes equations was selected since, firstly, complications arising from the pressure treatment in primitive formulation are circumvented and, secondly, because this form is readily extendible to three dimensions.

If $(\bar{\xi}, \bar{\eta}, \bar{\zeta})$ is the basic flow vorticity vector, $(\hat{u}, \hat{v}, \hat{w})$ is the velocity vector of the perturbed flow and $(\hat{\xi}, \hat{\eta}, \hat{\zeta})$ that of the perturbation vorticity, the perturbation equations are

$$\frac{\partial^2 \hat{u}^*}{\partial y^2} - \beta^2 \hat{u}^* - \mathrm{i}\beta\hat{\eta}^* - \frac{\partial \hat{\zeta}^*}{\partial y} = 0, \tag{2.7}$$

$$\frac{\partial^2 \hat{v}^*}{\partial y^2} - \beta^2 \hat{v}^* + \mathrm{i}\beta\hat{\xi}^* + \hat{\zeta}^* = 0, \tag{2.8}$$

$$\frac{\partial^2 \hat{w}^*}{\partial y^2} - \beta^2 \hat{w}^* + \hat{\eta}^* - \frac{\partial \hat{\xi}^*}{\partial y} = 0, \tag{2.9}$$

$$Re^{-1}\left\{\frac{\partial^2 \hat{\xi}^*}{\partial y^2} - \beta^2\hat{\xi}^*\right\} - \frac{\partial \hat{\xi}^*}{\partial t} - \bar{v}\frac{\partial \hat{\xi}^*}{\partial y} - \hat{v}^*\frac{\mathrm{d}\bar{\xi}}{\mathrm{d}y} - \mathrm{i}\beta\bar{w}\hat{\xi}^* + \bar{u}\hat{\xi}^* + \bar{\xi}\hat{u}^* = (\mathrm{RHS1})^*, \tag{2.10}$$

$$Re^{-1}\left\{\frac{\partial^2 \hat{\eta}^*}{\partial y^2} - \beta^2\hat{\eta}^*\right\} - \frac{\partial \hat{\eta}^*}{\partial t} - \bar{v}\frac{\partial \hat{\eta}^*}{\partial y} + \hat{\eta}^*\frac{\mathrm{d}\bar{v}}{\mathrm{d}y} - \mathrm{i}\beta\bar{w}\hat{\eta}^* - \bar{u}\hat{\eta}^* - \mathrm{i}\beta\bar{u}'\hat{v}^* = (\mathrm{RHS2})^*, \tag{2.11}$$

$$Re^{-1}\left\{\frac{\partial^2 \hat{\zeta}^*}{\partial y^2} - \beta^2\hat{\zeta}^*\right\} - \frac{\partial \hat{\zeta}^*}{\partial t} - \bar{v}\frac{\partial \hat{\zeta}^*}{\partial y} - \hat{v}^*\frac{\mathrm{d}\bar{u}'}{\mathrm{d}y} - \mathrm{i}\beta\bar{w}\hat{\zeta}^* - \bar{u}\hat{\zeta}^* - \bar{u}'\hat{u}^* + \mathrm{i}\beta\bar{u}'\hat{w}^* - \frac{\mathrm{d}\bar{w}}{\mathrm{d}y}\hat{\eta}^* = (\mathrm{RHS3})^*, \tag{2.12}$$

where a star superscript denotes a spectral (Fourier) space coefficient and RHS1–

RHS3 are the quadratic right-hand sides to the equations, which read

$$\mathrm{RHS1} = \hat{v}\,\frac{\partial\hat{\xi}}{\partial y} + \hat{w}\,\frac{\partial\hat{\xi}}{\partial z} - \hat{\xi}\,\hat{u}, \tag{2.13}$$

$$\mathrm{RHS2} = \hat{v}\,\frac{\partial\hat{\eta}}{\partial y} + \hat{w}\,\frac{\partial\hat{\eta}}{\partial z} + \hat{u}\,\hat{\eta} - \hat{\eta}\,\frac{\partial\hat{v}}{\partial y} + \hat{\zeta}\,\frac{\partial\hat{v}}{\partial z}, \tag{2.14}$$

$$\mathrm{RHS3} = \hat{v}\,\frac{\partial\hat{\zeta}}{\partial y} + \hat{w}\,\frac{\partial\hat{\zeta}}{\partial z} + \hat{u}\,\hat{\zeta} + \hat{\eta}\,\frac{\partial\hat{w}}{\partial y} - \hat{\zeta}\,\frac{\partial\hat{w}}{\partial z}. \tag{2.15}$$

The nonlinear terms are set identically equal to zero in the linear version of the code, to be reinstalled for mode-interaction studies. It is worth noting that, in view of the GH assumption, the $x$-dependence of this system has been eliminated. This confines the study to two dimensions and prohibits following the flow into turbulence. No-slip boundary conditions for the $x$- and $z$-components of the velocity are imposed and the definition of vorticity is used to derive boundary conditions for the vorticity. The normal-perturbation velocity component will be utilized to force the calculations in a manner which will be described later. Taking the far-field edge of the integration domain at a long distance from the wall, we impose vanishing of the perturbations at $y = y_\infty$. For linear computations in the neighbourhood of Branch II, in view of the far-field behaviour of the perturbations, we use $y_\infty = 25$; otherwise $y_\infty > 50$ is chosen. Computations are performed in boxes of variable spanwise extent, a typical combination of minimum spanwise wavenumber value and number of nodes utilized in this direction being $\beta_{min} \approx 4.5 \times 10^{-3}$ with $Nz = 256$.

### 2.3. *Spectral collocation solutions to the eigenvalue problem*

The results of the temporal eigenvalue problem formulated and solved by Hall *et al.* (1984) have been reproduced by Theofilis (1993) using the linear perturbation limit of (2.7)–(2.12). The solution approach utilized in the latter work was essentially the same as that used for the linear initial-boundary-value problem, although time was treated as a parameter. Second-order-accurate finite differences on a uniform grid were used in the wall normal. Theofilis (1995) presented a direct global spatial solution of the eigenvalue problem which permits the imposition of a variety of boundary conditions at infinity, including those of exponential decay that all eigenvalue problem work to date has utilized. Here, we proceed to obtain a solution to the temporal eigenvalue problem presented by Hall *et al.* (1984) utilizing the spectral collocation algorithm used for the spatial problem. Thus comparisons are possible between the linear initial-boundary-value problem results and those of a solution of the eigenvalue problem, although they are obtained using different numerical discretization algorithms and grids. The quality of the initial-boundary-value problem solution and, implicitly, its ability to address the question of nonlinear development of the linear GH solutions may thus be assessed. Further, we address the crucial question of the relevance of the GH linear theory to experimental results by use of the temporal-to-spatial transformation (Gaster 1962) of our temporal numerical results. On these we superimpose the spatial linear results of Theofilis (1995) and the new experimental data of Poll *et al.* (1996). A full account of the comparisons of the eigenvalue problem solutions and the aforementioned experimental results is currently in preparation and will be reported separately.

The eigenvalue problem may be expressed in terms of the streamwise $\hat{u}$ and normal $\hat{v}$ perturbation velocity components by the following system:

$$\left\{\mathscr{D}^2 - \overline{v}\mathscr{D} - \beta^2 - 2\overline{u} - \mathrm{i}\beta Re\overline{w}\right\}\hat{u} - (\mathscr{D}\overline{u})\,\hat{v} = -\mathrm{i}\beta Re\, c\,\hat{u}, \tag{2.16}$$

$$\begin{aligned}\{2(\mathscr{D}\overline{u}) + 2\overline{u}\mathscr{D}\}\,\hat{u} + \left\{\mathscr{D}^4 - \overline{v}\mathscr{D}^3 + \left[-2\beta^2 - \mathrm{i}\beta Re\overline{w} - (\mathscr{D}\overline{v})\right]\mathscr{D}^2\right.\\ + \left[\beta^2\overline{v} + (\mathscr{D}\overline{u})\right]\mathscr{D} + \beta^4 + \mathrm{i}\beta^3 Re\overline{w} + \mathrm{i}\beta Re\left(\mathscr{D}^2\overline{w}\right)\\ \left. + \beta^2(\mathscr{D}\overline{v}) + \left(\mathscr{D}^2\overline{u}\right)\right\}\hat{v} = -\mathrm{i}\beta Re\, c\,\left\{\mathscr{D}^2 - \beta^2\right\}\hat{v},\end{aligned} \tag{2.17}$$

with $\mathscr{D} = \mathrm{d}/\mathrm{d}\eta$ and $\eta$ defined in §2.1. The boundary conditions associated with this system are zero perturbations at the wall $\eta = 0$, while in the far field we may impose vanishing of perturbations, at sufficiently large a distance from the wall, or utilize the asymptotic form of the equations in this limit. Hall *et al.* (1984) demonstrated that the proper rate of decay for the perturbations in the far field is imposed if

$$\eta \to \infty : \qquad \hat{u} \sim \mathrm{e}^{-\eta^2/2}, \qquad \hat{v} \sim \mathrm{e}^{-\beta\eta}.$$

In the results that follow both options have been used and it was found that imposition of zero perturbations at a large finite distance yields eigenfunctions with the asymptotic behaviour shown above. Hall *et al.* (1984) solved this problem using a compact finite-difference scheme and it is desirable to obtain the solution to (2.16)–(2.17) using a different numerical approach. Here we solve the eigenvalue problem using spectral collocation based on Chebyshev polynomials. Orszag (1971) demonstrated that a Chebyshev-tau approach is ideally suited to tackle hydrodynamic stability problems. The first spectral collocation solution to temporal eigenvalue problems pertinent to the (compressible) Navier–Stokes equations to appear in the literature was the work of Macaraeg, Streett & Hussaini (1988). There it was shown that a collocation approach also yields highly accurate frequency and growth rate results at a minimal number of nodes compared to standard finite-difference discretizations. Moreover, in the incompressible limit a very small number of nodes guaranteed a converged solution to within very small tolerance. Utilization of as small as possible a number of nodes is necessary in solving the generalized eigenvalue problem globally, given the cost of the QZ algorithm invariably used for this type of problem (Wilkinson 1965) which scales with the cube of the number of nodes utilized. The system (2.16)–(2.17) takes the form of a generalized eigenvalue problem for the determination of the eigenvalue $c$ once a prescription for the discrete approximation of the derivative $\mathscr{D}$ has been provided. We combine domain truncation with mapping and incorporate the metrics of the transformation into the standard Chebyshev collocation derivative matrices in order to form approximations to the first four derivatives required in (2.16)–(2.17). Some details of the solution method are presented in Appendix A.

Eigenvalue problem results have been obtained for a number of values of the suction parameter, although in the nonlinear computations that follow only those pertinent to zero suction will be utilized. In figure 2 the neutral curves for $\kappa = -0.1, 0$ (0.2) 0.8 are presented in $(Re, \beta)$ space. Superimposed is the (graphically reproduced) result for the zero-suction neutral loop presented by Hall *et al.* (1984). Line-thickness agreement may be seen between the neutral loop of Hall *et al.* and the present result. In table 1 we present our grid refinement history for the complex eigenvalue at the neutral conditions of Hall *et al.*; using the aforementioned global spectral algorithm and 64 Chebyshev collocation nodes the discrepancy between the results of Hall *et al.* and our calculations is less than $1 \times 10^{-6}$, the former investigators having used 160 points in their iterative finite-difference solution to predict a neutral frequency

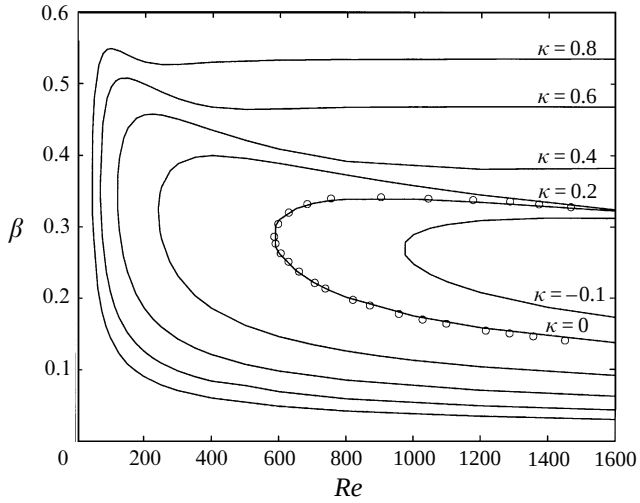


FIGURE 2. The temporal eigenvalue problem neutral loops in $(Re, \beta)$ space. Inner to outer loop corresponds to suction parameters $\kappa = -0.1, 0, (0.2), 0.8$. Superimposed upon the $\kappa = 0$ result and denoted by 'o' the zero suction result of Hall *et al.* (1984).

| | $\kappa = 0$, $Re = 800$ | | $\kappa = 0.18$, $Re = 350$ | |
|---|---|---|---|---|
| $N$ | $\omega_r$ | $\omega_i$ | $\omega_r$ | $\omega_i$ |
| 16 | 0.131390 | −0.000357 | 0.125923 | 0.003497 |
| 32 | 0.127072 | −0.000024 | 0.125446 | 0.002515 |
| 64 | 0.127098 | 0.000000 | 0.125442 | 0.002509 |

TABLE 1. Grid refinement history in the numerical solution of the temporal eigenvalue problem at $\kappa = 0$, $Re = 800$, $\beta = 0.3384638$ (compact finite-difference result (Hall *et al.* 1984) $\beta c_r = 0.1270977$) and at $\kappa = 0.18$, $Re = 350$, $\beta = 0.3053125$ (Poll *et al.* 1996).

of $c_r = 0.3755134$. For comparison with recent experimental results of Poll *et al.* (1996) in table 1 we also present the convergence history of the temporal growth rate of the maximally amplified wave at $Re = 350, \kappa = 0.18$; at these parameters the boundary layer has a displacement thickness $\delta^* = 1.143159$ and a momentum thickness $\theta = 0.432980$. The wavenumber of the most unstable wave, $\beta = 0.3053125$, was determined by cubic spline interpolation of the $\beta$ vs. $\omega_i$ linear theory result. It may be seen in these results also that 64 collocation points are sufficient for converged frequency and growth rate results to be obtained. The spatial structure of the $\hat{u}$ and $\hat{v}$ eigenfunctions at zero-suction critical conditions $Re = 583.1, \beta = 0.288$ (Hall *et al.* 1984) is presented in figures 3(*a*) and 3(*b*) for the normalized $\hat{u}$ and $\hat{v}$ respectively. Worth noticing in this figure is the rate of decay of perturbations at infinity, which is characteristic of incompressible boundary layers; this result will be taken into account in the direct numerical simulations that follow.

### 2.4. *Convergence of the DNS results and comparison with linear stability theory*

Direct numerical simulations of flat-plate boundary layers, either incompressible (Laurien & Kleiser 1989) or compressible (Adams 1993), have established that a minimum prerequisite for credibility of (nonlinear) DNS results is the reproduction by DNS of the frequency and growth rate results of linear stability theory. Here,

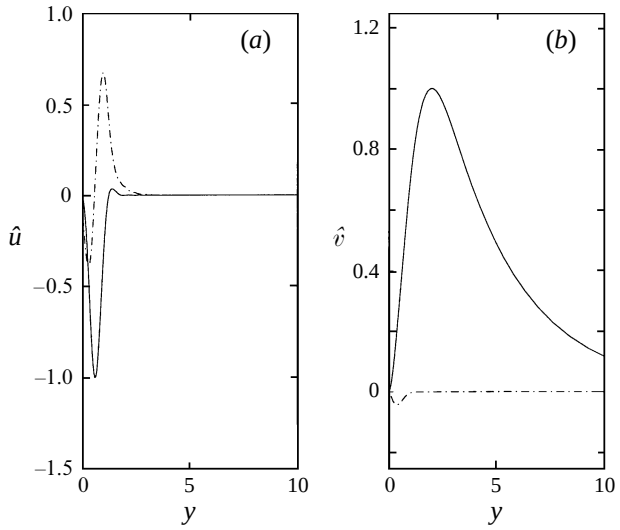


FIGURE 3. Neutral eigenfunctions for $\kappa = 0$. In ($a$), solid: Re$\{\hat{u}\}$, dashed Im$\{\hat{u}\}$. In ($b$), solid: Re$\{\hat{v}\}$, dashed Im$\{\hat{v}\}$.

| $Ny$ | $y_2 \times 100$ | $\omega_r$ | $\omega_i$ |
|---|---|---|---|
| 51 | 1.215 | 0.125567 | 0.002408 |
| 101 | 0.601 | 0.125450 | 0.002485 |
| 151 | 0.399 | 0.125447 | 0.002498 |
| 201 | 0.299 | 0.125441 | 0.002503 |
| 251 | 0.239 | 0.125443 | 0.002505 |
| 301 | 0.199 | 0.125442 | 0.002506 |
| 351 | 0.171 | 0.125439 | 0.002507 |
| 401 | 0.149 | 0.125434 | 0.002507 |

TABLE 2. Grid refinement in the numerical solution of (2.7)–(2.15) at $\kappa = 0.18$, $Re = 350$, $\beta = 0.3053125$.

we subject our nonlinear initial-boundary-value problem code for the incompressible attachment-line boundary layer to this test. A comment is in order at this point on the means by which linear stability theory information is extracted from the time-dependent DNS results. During linear growth the exponential time behaviour of the solution is utilized either explicitly or in terms of a logarithmic derivative of any flow quantity; three alternatives have been used to recover the results that follow which, at convergence, are identical to each other. Details may be found in Appendix B.

The grid sequencing at conditions chosen to correspond to the $\kappa = 0.18$ boundary layer presented in table 1 may be found in table 2. Shown are the number $Ny$ of the non-uniformly distributed finite-difference points in the wall-normal direction, the location of the first point off the wall $y_2$ and the frequency $\omega_r$ and growth rate $\omega_i$ during linear growth, calculated using method 2 described in Appendix B. Convergence of the fourth decimal place may be seen to have been achieved in the DNS results at $Ny > 200$. As an aside, on the technical level, one notices a further demonstration of the well-known fact in transition simulation that finite-difference types of methods typically require an order of magnitude larger number of points

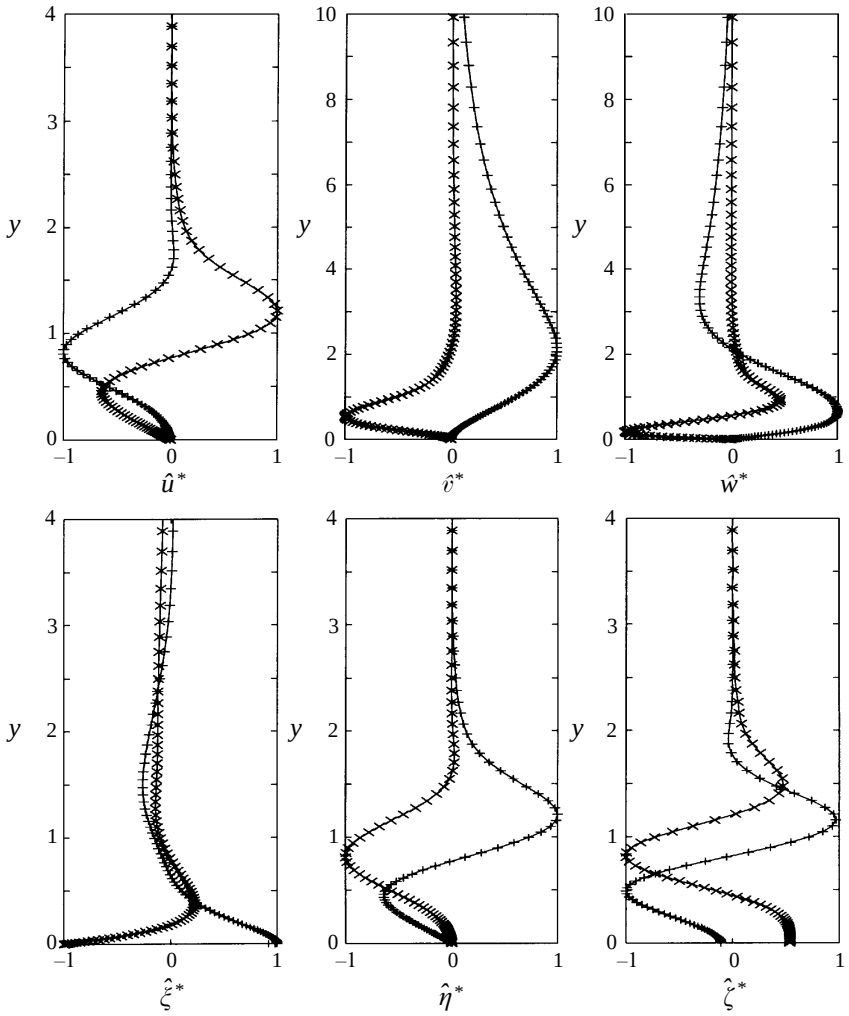


FIGURE 4. Linear eigenfunctions at $\kappa = 0.18$, $Re = 350$, $\beta = 0.3053125$ predicted by DNS (solid) and their comparison against the linear stability theory result. Symbol $+$: real part; symbol $\times$: imaginary part.

to achieve the converged result compared with that needed by a spectral simulation. The overall cost of the algorithm in two dimensions, however, is determined by the cost of inverting the matrix in which the discrete form of the governing equations is cast; in this respect the significantly lower cost of inverting the banded matrix which results from a finite-difference discretization compared to that of inverting the dense matrix resulting from a spectral method may compensate for the additional number of nodes utilized in the former scheme.

The result of major significance, though, is the agreement between the linear theory result presented in table 1 and the converged direct simulation result of table 2. Against a background of different systems of equations being solved, using a spectral method for the eigenvalue problem as opposed to finite differences in the DNS, and the grids on which the respective solutions have been obtained being different, the relative discrepancy between the frequency and growth rate delivered

by the eigenvalue problem and the respective converged DNS result is less than 0.01% for the frequency and 0.1% for the growth rate. The spatial structure of the disturbance vector obtained at this wavenumber parameter is presented in figure 4. Solid lines denote the normalized DNS result for the real and imaginary parts of velocity and vorticity Fourier coefficients upon which the respective normalized real (+) and imaginary (×) parts calculated by solution of the eigenvalue problem are superimposed. Numerical solution of the eigenvalue problem delivers the chordwise $\hat{u}$ and normal $\hat{v}$ disturbance velocity components as the eigenvector; we post-calculate the spanwise disturbance velocity component $\hat{w}$ using the equation of continuity for this flow

$$\hat{u} + \mathscr{D}\hat{v} + \mathrm{i}\beta\hat{w} = 0,$$

and the three vorticity components using the definition of disturbance vorticity

$$\hat{\xi} = \mathscr{D}\hat{w} - \mathrm{i}\beta\hat{v}, \hat{\eta} = \mathrm{i}\beta\hat{u}, \hat{\zeta} = -\mathscr{D}\hat{u}.$$

Aside from the agreement between linear stability theory and DNS results which corresponds to that exhibited by the frequency and growth rate results, a number of other points are worthy of mention in this figure. First, the spanwise disturbance velocity component has the typical structure of a Tollmien–Schlichting instability propagating in the streamwise direction in the two-dimensional Blasius boundary layer. It is this fact which led investigators in the past to attempt to use the non-rationally obtained Orr–Sommerfeld equation to describe instability along the spanwise direction in the attachment-line boundary layer. Second, a comparison of the rates of decay of the normal velocity component in the far field, for which homogeneous boundary conditions have been imposed in our DNS, confirms the prediction of Hall *et al.* (1984) regarding the rate of decay utilized in their eigenvalue problem solution. Third, credibility is given to the numerical treatment of (2.7)–(2.15) with respect to the boundary conditions on vorticity, an issue which has been extensively discussed in the past in the context of incompressible direct numerical simulations; utilizing the definition of vorticity to derive boundary conditions for its three components delivers results which show excellent agreement with those obtained by numerical differentiation of the eigenvalue problem results. The wall-normal disturbance vorticity component is predicted to be a multiple of the chordwise disturbance velocity component, while the chordwise and spanwise disturbance vorticity components delivered by DNS have wall values that agree with those predicted by the eigenvalue problem to the same high accuracy as the respective eigenvalues.

Next we monitor the agreement between DNS results and linear theory at different parameter values. In table 3 we present comparisons at two further representative Reynolds number values, one at which the flow is linearly unstable, $Re = 800$, and one in the middle of the disputed linearly subcritical region, $Re = 550$. DNS results were obtained at the modest wall-normal resolution which was found to deliver acceptable accuracy, $Ny = 251$. The comparisons of DNS with the linear theory results at all parameter values attempted was found to be as favourable as that presented at maximum growth conditions in the $Re = 350$, $\kappa = 0.18$ boundary layer. In the latter flow one sees in table 3 that the region of instability delienated by DNS is that which the eigenvalue problem predicts and the small-amplitude linear waves resulting from the simulations are identical to those that may be calculated using linear theory. An analogous conclusion on both the location of the branches of the neutral loop and the values of frequency and growth rate may be drawn for the linearly unstable $Re = 800$. Small-amplitude disturbances at $Re = 550$, on the other hand, are found

$Re = 350, \kappa = 0.18$

| | DNS | | LST | |
|---|---|---|---|---|
| $\beta$ | $\omega_r$ | $\omega_i$ | $\omega_r$ | $\omega_i$ |
| 0.15625 | 0.054865 | −0.003462 | 0.054886 | −0.003444 |
| 0.18750 | 0.069076 | −0.001568 | 0.069087 | −0.001550 |
| 0.21875 | 0.083677 | 0.000163 | 0.083683 | 0.000168 |
| 0.25000 | 0.098574 | 0.001487 | 0.098578 | 0.001498 |
| 0.28125 | 0.113692 | 0.002297 | 0.113695 | 0.002304 |
| 0.31250 | 0.128958 | 0.002491 | 0.128962 | 0.002495 |
| 0.34375 | 0.144300 | 0.002003 | 0.144307 | 0.002003 |
| 0.37500 | 0.159645 | 0.000782 | 0.159655 | 0.000777 |
| 0.40625 | 0.174913 | −0.001216 | 0.174928 | −0.001225 |
| 0.43750 | 0.190017 | −0.004028 | 0.190039 | −0.004042 |

$Re = 550, \kappa = 0$

| | DNS | | LST | |
|---|---|---|---|---|
| $\beta$ | $\omega_r$ | $\omega_i$ | $\omega_r$ | $\omega_i$ |
| 0.12500 | 0.039903 | −0.005837 | 0.039925 | −0.005827 |
| 0.15625 | 0.052836 | −0.004565 | 0.052845 | −0.004550 |
| 0.18750 | 0.066233 | −0.003106 | 0.066234 | −0.003093 |
| 0.21875 | 0.079944 | −0.001795 | 0.079938 | −0.001787 |
| 0.25000 | 0.093884 | −0.000844 | 0.093876 | −0.000841 |
| 0.28125 | 0.107984 | −0.000386 | 0.107975 | −0.000387 |
| 0.31250 | 0.122173 | −0.000508 | 0.122164 | −0.000515 |
| 0.34375 | 0.136375 | −0.001272 | 0.136367 | −0.001285 |
| 0.37500 | 0.150507 | −0.002722 | 0.150501 | −0.002740 |

$Re = 800, \kappa = 0$

| | DNS | | LST | |
|---|---|---|---|---|
| $\beta$ | $\omega_r$ | $\omega_i$ | $\omega_r$ | $\omega_i$ |
| 0.12500 | 0.038241 | −0.003809 | 0.038253 | −0.003796 |
| 0.15625 | 0.050511 | −0.002203 | 0.050511 | −0.002191 |
| 0.18750 | 0.063164 | −0.000613 | 0.063155 | −0.000605 |
| 0.21875 | 0.076112 | 0.000658 | 0.076098 | 0.000659 |
| 0.25000 | 0.089287 | 0.001430 | 0.089270 | 0.001425 |
| 0.28125 | 0.102613 | 0.001588 | 0.102596 | 0.001576 |
| 0.31250 | 0.116005 | 0.001048 | 0.115988 | 0.001030 |
| 0.34375 | 0.129367 | −0.000261 | 0.129351 | −0.000271 |
| 0.37500 | 0.142586 | −0.002362 | 0.142573 | −0.002395 |

TABLE 3. Frequency and growth rate DNS results obtained during linear growth, compared with linear stability theory (LST) results.

to be linearly stable, again the discrepancy between linear theory and the moderately resolved DNS results being of the order of a few tenths of a percent.

Having established agreement between the well-accepted eigenvalue problem and the current DNS results, we turn to comparisons of the latter during linear growth with the new experimental results for the flow in question obtained by Poll *et al.* (1996). In this context we stress that to date all experimental work has provided information only on the frequency of the observed instability waves. No growth rates have ever been presented, nor the spatial structure of disturbances. Consequently, statements on the agreement of the various theories put forward with experiment are only possible through comparison of the frequency results. This situation is

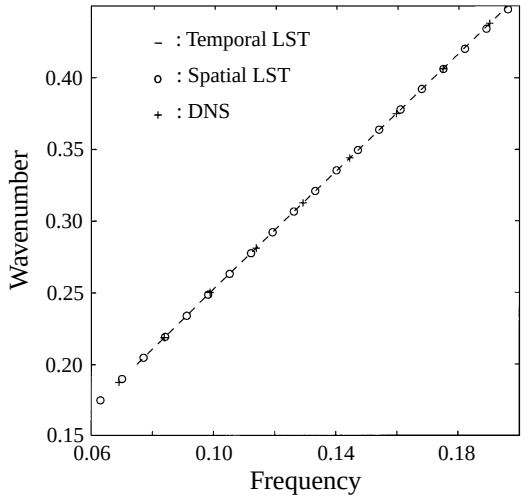


FIGURE 5. Wavenumbers against frequency of naturally occurring waves predicted by the DNS and compared with those yielded by temporal and spatial linear stability analyses at $Re = 350$, $\kappa = 0.18$.

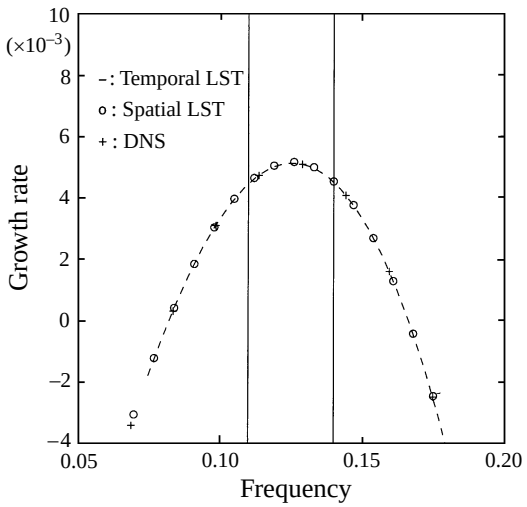


FIGURE 6. Growth rate against frequency of naturally occurring waves predicted by the DNS and compared with those yielded by temporal and spatial linear stability analyses at $Re = 350$, $\kappa = 0.18$. Unstable waves have been measured by Poll *et al.* (1996) having a frequency between the two vertical lines.

quite unlike the progress that has been made in the classical flat-plate boundary layer; substantially more experimental information is necessary in the flow under consideration for further advances in theory.

In figure 5 the wavenumbers of the predicted waves are presented as a function of their frequency. All three approaches utilized, namely temporal and spatial eigenvalue problem, and (temporal) DNS, are capable of identifying the unstable mode with high accuracy; the temporal eigenvalue problem and DNS results agree to 6 significant places and define a linear relationship between the quantities monitored. Spatial eigenvalue problem results are in line-thickness agreement with the Gaster-transformed temporal results. Turning to the growth rates of the instability waves predicted, we

present in figure 6 the frequency range of maximally amplified waves measured by Poll *et al.* (1996), between the vertical lines; the width of this area corresponds to the error bar of the experimental results. Superimposed upon the experimental data are our results for the eigenproblem as well as the growth rate delivered by DNS. It may be seen in this figure that the spatial and the Gaster-transformed temporal results agree very well with each other in both the value of the maximum growth rate calculated, and the identification of the location, in parameter space, of the branches of the neutral loop. Line-thickness agreement between the spatial eigenvalue problem and the transformed temporal eigenvalue problem and DNS results is to be found in the neighbourhood of the neutral points, while the spatial eigenvalue problem predicts marginally higher growth rates than those calculated by the temporal approaches at conditions of maximum growth. It has to be noted that this very good performance of the Gaster transformation of temporal results is a consequence of the small values of the growth rates encountered in this problem.

In summary, we have demonstrated that the initial-boundary-value problem formulation (2.7)–(2.15) firstly delivers linear results in remarkable agreement with those yielded by the eigenvalue problem and secondly is capable of predicting the experimentally observed instability waves of small amplitude in the swept attachment-line boundary layer. Not only does the agreement between eigenvalue problem and initial-boundary-value problem results constitute a generalization of the former approach but it also lends credibility to the proposal that results relevant to experimental observations may be obtained by studying the nonlinear evolution of linear initial-boundary-value problem perturbations. The level of agreement shown is actually the only firm indication that the nonlinear solutions to be obtained in what follows are of relevance to the physical problem considered.

## 3. The nonlinear evolution of Görtler–Hämmerlin disturbances in LEBL flow

We next turn our attention exclusively to the numerical solution of system (2.7)–(2.15), allowing for mode interaction, and briefly describe the algorithm utilized. The nonlinear terms RHS1–RHS3 are included in a scheme which simultaneously solves for a range of wavenumbers of interest at a given Reynolds number value. To this end, a mapping in the wall-normal direction is incorporated into the finite-difference numerical solution approach presented in Theofilis (1993), which distributes points across the layer according to

$$y = C\,\frac{y'}{1 + C/L_y - y'} \tag{3.1}$$

with $y' \in [0,1]$. $L_y$ is the extent of the calculation domain in the wall-normal direction, non-dimensionalized with respect to $\Delta$. In view of the stretching transformation, there is no implementational difficulty in extending the upper limit of the wall-normal calculation domain far outside the boundary layer so that the imposition of zero-perturbation boundary conditions is permissible. It is worth noting here that Hall & Malik (1986) asserted that imposition of zero-perturbation boundary conditions on the perturbation velocities at the edge of the computational domain $y_\infty = 15$ produced identical results to those obtained by using the boundary conditions stemming from the discussion of §2.3. However, we chose the safer option of placing the outer computational boundary very far from the layer, in view of both the sensitivity of growth rate results to 'pinching' the basic flow and the boundary conditions used. $C$ is

a parameter used to control the stretching, assuming the value $C = 0.5$ for the present calculations. It should be noted at this point that, although there is no real justification in using numerical schemes of low formal accuracy for stability calculations, the treatment of the wall-normal direction with finite differences alongside the implicit scheme used for time-integration outlined next differentiate our numerical approach from that of both Hall & Malik (1986) and Jiménez *et al.* (1990) and we wish to maintain our numerical methods as distinct as possible from those of other investigators.

The spanwise direction along the attachment line was treated pseudospectrally, employing a Fourier expansion over a periodicity length $L_z$. This approach is dictated by the flow physics, namely the homogeneity of the flow in this direction. Aside from the superior accuracy properties of a spectral expansion compared to a finite-difference treatment, the former has the added advantage of being ideally suited for mode interaction studies. Nonlinearities were evaluated by transform methods, with dealiasing incorporated (but not necessarily used; details follow). Fast as well as direct Fourier transforms have been used and the Hermitian property of the spectral space solution has been exploited in order to keep the computing cost to a minimal. Time integration was performed by a second-order-accurate Crank–Nicolson scheme, in view of the time-step limitations imposed by the CFL condition in conjunction with the fine wall-normal resolution, were an explicit scheme to be utilized. Vector implementation of library software (Numerical Algorithms Group, 1992) was utilized for the residual calculations.

It is noted that use of an implicit scheme for time integration was initially expected to result in an algorithm more expensive overall than that resulting from utilization of a fully explicit scheme, especially if long-time integration were to be performed. The rather small values of $y_2$ shown in table 2, however, suggest that a scheme combining explicit and implicit time integration is probably a better candidate than a fully explicit scheme in order to replace the Crank–Nicolson scheme used here; factors such as hardware architecture and library software implementation may also play a role in such a decision, which would only be taken if the present algorithm were to be extended to three dimensions. At present, we are only interested in the early-time results, as the two-dimensional model considered in this paper does not permit following the flow into turbulence, and the implicit time integration was found to perform quite adequately. The reader is referred to Duck & Burggraf (1986) as well as Theofilis (1993) for further details on the numerical algorithm.

The solution is initially forced by utilizing the wall-normal perturbation velocity component $\hat{v}^*(y = 0, \beta, t)$ in a way such that two physical situations may be modelled. We take $\hat{v}^*(0)$ to be of the generic form

$$\hat{v}^*(y = 0, \beta, t) = \varepsilon \; H_0(t) \; F(t) \, \mathrm{e}^{-\beta^2}. \tag{3.2}$$

In both cases $\varepsilon$ is an $O(1)$ amplitude parameter, utilized to control the magnitude of the forcing applied to the normal component of the velocity. The functional dependence $F(t)$ is utilized to differentiate between the modelled cases; the specific forms will be discussed below. In order to avoid potentially slower than exponential convergence, had we used a more involved dependence of $\hat{v}^*(y = 0, \beta, t)$ on the spanwise wavenumber, we adhered to the simple error-function type of excitation. Finally, $H_0(t)$ is a unit step function indicating the finite startup time of our calculations, defined by

$$H_0(t) = \begin{cases} 0, & t < 0 \\ 1, & t \geqslant 0. \end{cases}$$

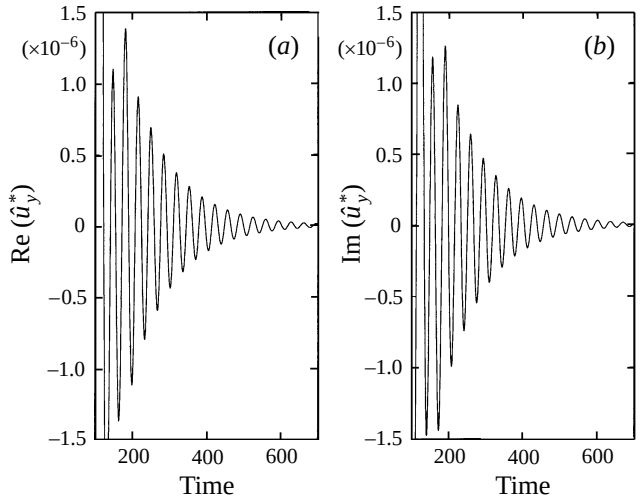


FIGURE 7. Wave emerging at $Re = 550, \beta = 0.3$. In (*a*) and (*b*), respectively, real and imaginary parts of perturbation wall shear $\hat{u}_y$ against time.

A comment is in order here regarding the increasing magnitude of the excitation. One has to ensure that the excitation is introduced into the flow smoothly in time so as to avoid numerical instability problems at the early stages of the calculations. As $\varepsilon$ is increased, this requirement translates into ever smaller initial time steps, rendering the numerical solution ever more expensive. The calculations are stopped when converged results for the growth rates of the two-dimensional instability waves have been obtained, usually after a small number of linear wave periods.

In the results that follow, typically, a ($Ny = 151 \times Nz = 256$) grid has been utilized, stretched in the normal direction so as to place the first field point at $y_2 \approx 10^{-3}$ away from the wall, while a zero-perturbation boundary condition was imposed at $y_\infty = 100$. The basic flow was obtained in this domain on $O(10^5)$ uniformly distributed nodes. The result was interpolated onto the calculation grid using cubic splines for reasonable accuracy; integral flow quantities were monitored and nodes on the calculation grid were distributed such that approximately eight significant figures in quantities such as displacement thickness and shape factor were preserved between the two grids.

The results of the linear and the nonlinear versions of the system (2.7)–(2.12) have been compared extensively against each other, using the jet-excitation form presented in the next section. A typical result is presented in figure 7: after some initial transient the solution at each wavenumber assumes the form of a wave, which may be compared to the predictions of linear theory. Values for the frequency $\mathrm{Re}\{\omega\}$ and the growth rate $\mathrm{Im}\{\omega\}$ are calculated either through the time signal of a wall shear in, say, spectral space using

$$\omega = \frac{1}{\hat{u}_y^*} \frac{\mathrm{d}\hat{u}_y^*}{\mathrm{d}t} \tag{3.3}$$

with $\hat{u}_y^* = \partial \hat{u}^* / \partial y$ ($y = 0, z = z_0, t$) or, equivalently, through monitoring a measure of the disturbance energy

$$E(\beta, t) = \int_0^{y_\infty} \{\hat{u}^2 + \hat{v}^2 + \hat{w}^2\} \, \mathrm{d}y \tag{3.4}$$

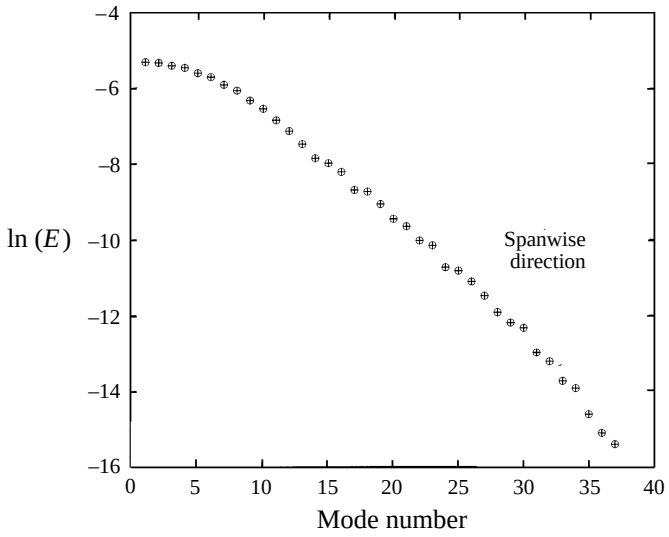


FIGURE 8. Spanwise resolution quality test.

and calculating the slope of the function

$$\ln\left(E(t)\right)^{1/2},$$

the two definitions yielding identical results; details may be found in Appendix B. The quantity defined in (3.4) is, additionally, significant in that it measures the strength of an individual Fourier component and, as such, may be monitored in relation to resolution requirements of the simulation. Such a study has been done in the course of the runs presented next and a typical result is presented in figure 8. Worth noticing here are firstly, the linear dependence of the logarithm of energy against mode number typical of spectral simulations. Secondly, it has been demonstrated (e.g. Canuto *et al.* 1988) that a minimum requirement for reliability of results obtained in a transition simulation is the separation of the energy, defined in (3.4), of the most-energetic from that of the least-energetic (Fourier) modes by at least eight orders of magnitude. More than ten orders of magnitude separation is demonstrated in figure 8; moreover, the typical tail in the energy spectrum which denotes imminent loss of accuracy due to accumulation of energy in the high-wavenumber region is absent from our calculations. As a consequence, it is irrelevant to actually invoke the dealiasing option in our simulations, since all scales are well resolved, resolution being far from marginal.

Turning to comparisons between the linear and nonlinear versions of (2.7)–(2.12) we first note that linearized results may be obtained at single values of the wavenumber $\beta$ at a cost slightly higher than that of the eigenproblem. In contrast, the nonlinear version of (2.7)–(2.12) is orders of magnitude more expensive on two counts. Firstly, the solution has to be obtained simultaneously for the full wavenumber range and secondly, the nonlinearities mandate iterations at each time step. Owing to the cost of the latter, a limited number of comparisons between the linear and the nonlinear forms of (2.7)–(2.12) was performed. A typical result for $\omega$ at $Re = 590$, $\beta = 0.3$ is presented in figure 9. It may be observed that both the time history and, more importantly, the converged result for both the frequency and the growth rate history of the wave predicted by the two schemes follow each other very closely. The dependence

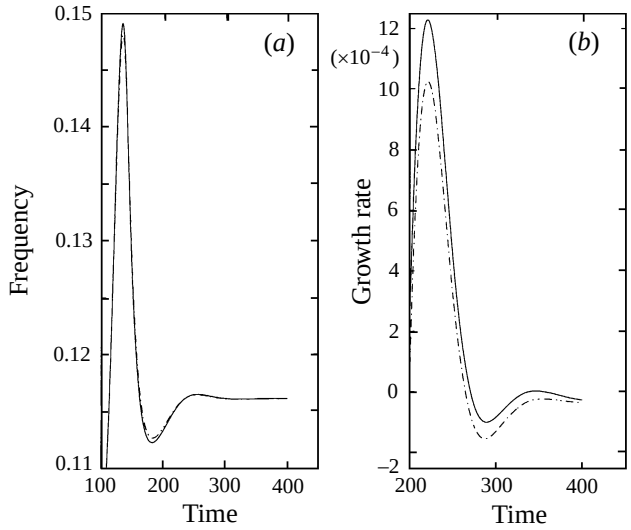


FIGURE 9. Frequency in (*a*) and growth rate in (*b*) against time at $Re = 590$, spanwise wavenumber $\beta = 0.3$ predicted by linear and nonlinear numerical solution of (2.7)–(2.12). Solid: nonlinear; Dashed: linear.

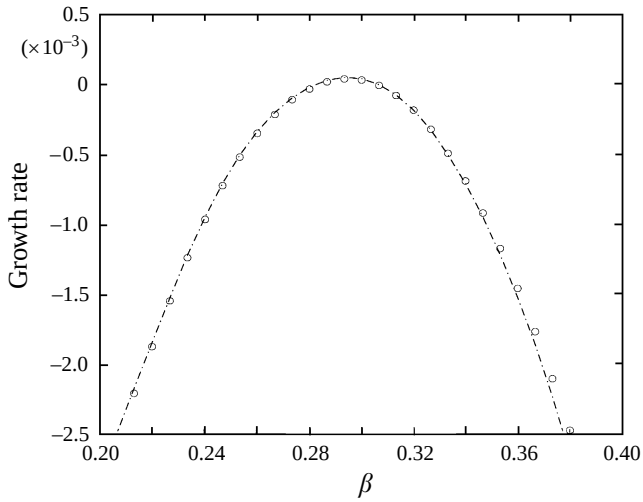


FIGURE 10. Linear (dashed) and nonlinear (symbols) growth rate against wavenumber at $Re = 590, t = 400$.

of $\omega_i$ on $\beta$ at a particular flow condition is presented in figure 10. The amplitude of initial excitation $\varepsilon$ has, of course, been kept the same in the two schemes and is taken to be of small magnitude in order for comparisons to be possible. The absence of interaction in the linear version of the initial-boundary-value problem results in unphysical results being obtained at the limit of very large time since there is no mechanism to control the linearly predicted exponential growth of disturbances. In contrast the nonlinear initial-boundary-value problem system produces disturbances that may interact and are seen, as time grows, to saturate; such a behaviour is presented in figure 11. In what follows, we focus exclusively on nonlinear initial-

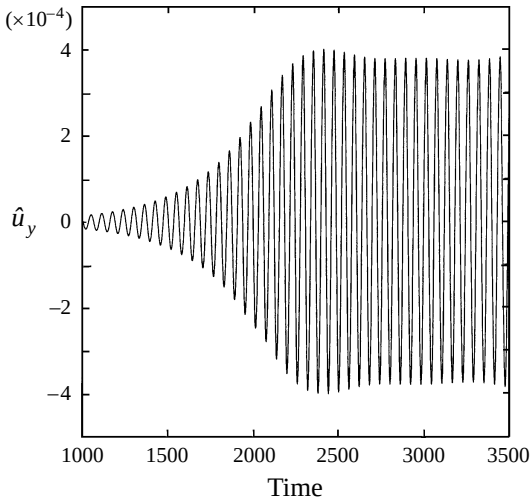


FIGURE 11. Nonlinear saturation of linearly unstable mode.

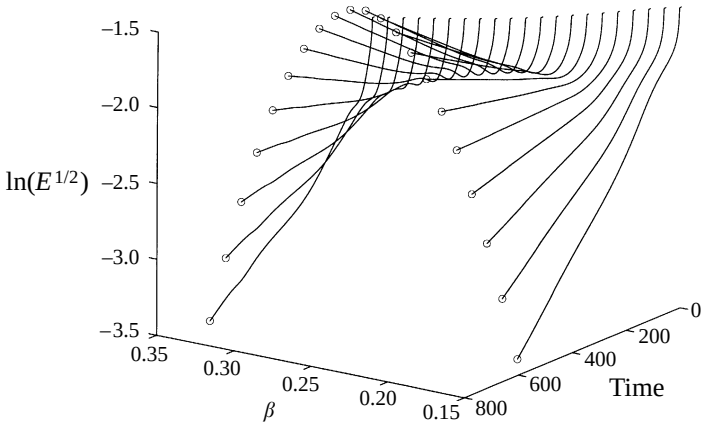


FIGURE 12. Perturbation energy as function of time at $Re = 800, \beta \in [0.15, 0.35]$.

boundary-value problem solutions which have been obtained utilizing two forms of initial excitations described below.

### 3.1. *A jet issuing from the wall*

Taking the function $F(t)$ in (3.2) to be smoothly growing and decaying in time, such as

$$F(t) = \tanh^2(t)\ (1 - \tanh^2(t)), \tag{3.5}$$

we enforce initial conditions on the initial-boundary-value problem which model the physical situation of a jet issuing from the wall. At $Re = 800$, we obtained a numerical solution subject to this initial condition and the perturbation energy has been monitored and plotted at $\varepsilon = 1$ in figure 12. Observations based on the results of this figure are, firstly, that the typical dependence of perturbation energy on time is present in our calculations; after an initial dip a linear regime follows. Secondly, the wavenumber region considered contains all unstable wavenumbers at this Reynolds

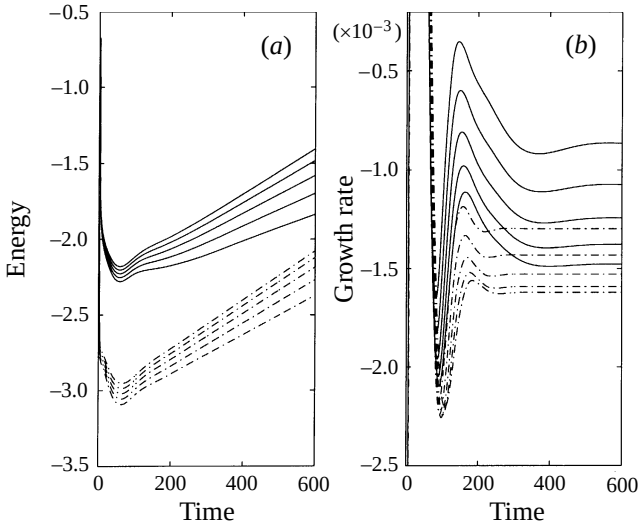


FIGURE 13. Nonlinear (solid) vs. linear (dashed) results at $Re = 800$. Lower to higher: spanwise wavenumber $\beta = 0.15\,(.01)\,0.19$.

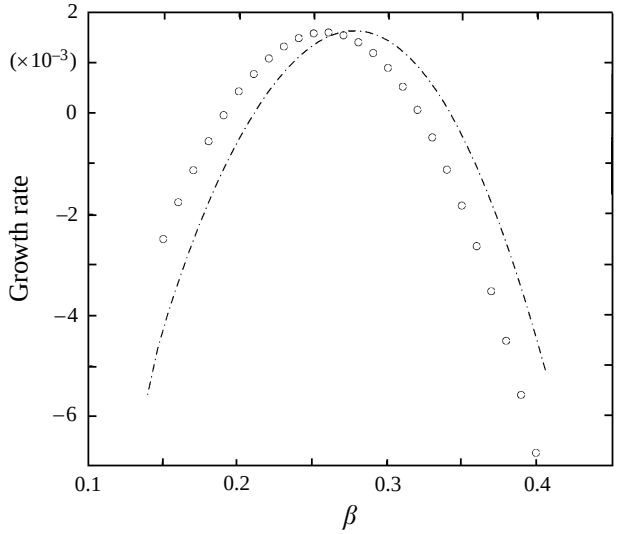


FIGURE 14. Linear (dashed) and nonlinear (symbols) growth rate dependence on wavenumber at $Re = 800$.

number; the exact location of Branch I and Branch II may be obtained as the projection on the wavenumber axis of the curves $E(t) = \text{const}$.

By experimenting with $\varepsilon$, nonlinear solutions have been obtained at $Re = 800$ that are discussed next. We present in figure 13 the (nonlinear) time evolution of $E$ in ($a$) and the corresponding growth rate in ($b$) and superimpose the respective linear results pertinent to wavenumbers in the neighbourhood of Branch I. It may be observed that a systematic departure exists between the linear and nonlinear results; this departure is a consequence of increasing $\varepsilon$ and is systematically to be observed as this imposed amplitude of excitation of the form (3.2) is increased. Care should be taken, in this

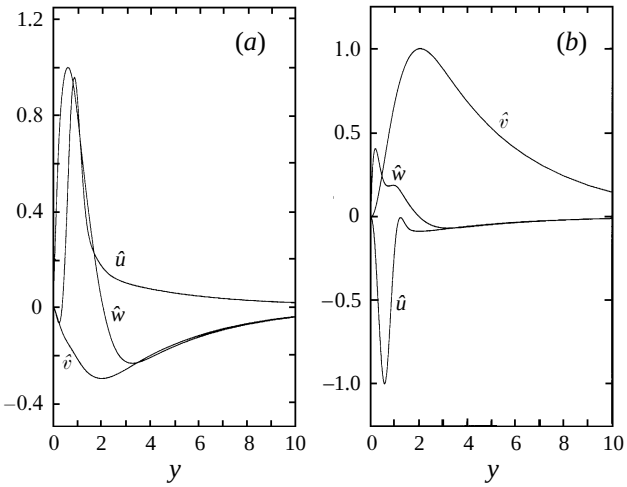


FIGURE 15. Nonlinear perturbations at maximum growth conditions at $Re = 800, \beta \approx 0.27$. ($a$) Real part. ($b$) Imaginary part.

context, in the interpretation of $\varepsilon$ when attempting to compare with experiments, where usually 'amplitude' denotes some quantity related to linear unstable waves, for example the r.m.s. value of a linear perturbation. We present in figure 14 at $\varepsilon = 10$ the growth rates pertinent to nonlinear perturbations of wavelengths $2\pi/\beta$ as function of $\beta$ at $Re = 800$ and compare with the linear result. Observations of significance are the following.

Firstly, nonlinear equilibrium solutions are obtained (corresponding to the zero-growth-rate nonlinear results in figure 14) that bifurcate supercritically from Branch I and subcritically from Branch II, as the weakly nonlinear analysis of Hall & Malik (1986) predicted; such a behaviour was also observed in the computations of Jiménez *et al.* (1990). Secondly, no appreciable difference of the level of the maximum growth rate may be seen between the linear and the nonlinear results: at $Re = 800$ the nonlinear solution at $\varepsilon = 10$ delivers practically the same maximum growth rate as the linear result. The spatial structure of perturbations at maximum growth conditions is presented in figure 15; the different rate of decay at infinity for the streamwise and normal perturbation velocities, typical of incompressible Navier–Stokes simulations and also predicted by the eigenvalue problem, is also exhibited in these nonlinear results.

Calculations performed at $\varepsilon = 10$ and Reynolds numbers $Re = 600, 700$ and $Re = 900$, as well as the result of figure 14 are superimposed upon the linear results and presented in figure 16. Only growing waves are presented ($\omega_i > 0$) and it may be inferred from the dependence of the maximum growth rate at a given Reynolds number on $Re$ that in the present nonlinear results the possibility of a (nonlinear) critical Reynolds number lower than that delivered by the linear analysis is excluded. As discussed already, the experimentally observed naturally occurring linear instability waves are located in the neighbourhood of Branch I. This is unlike the classical Blasius boundary layer, where the experimentally observed instabilities peak between the lines of maximum amplification rate and maximum amplitude ratio. In a nonlinear framework, the theory of Hall & Malik (1986) demonstrated that, apart from a small interval near the tip of the neutral loop, the solution bifurcates supercritically from Branch I and subcritically from Branch II. The former

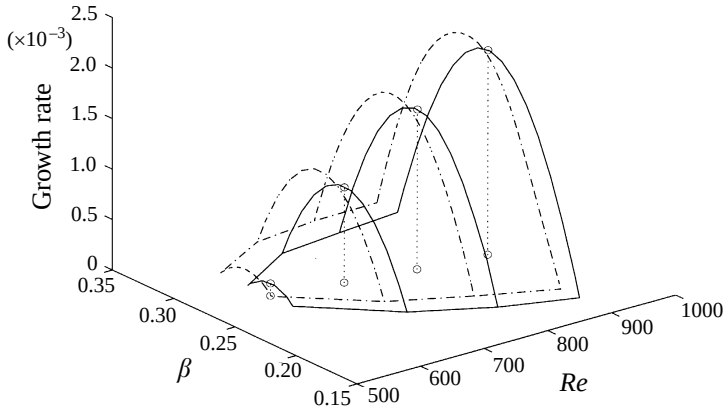


FIGURE 16. Nonlinear (solid) vs. linear (dashed) neutral loops; projected is the line of maximum amplification rate.

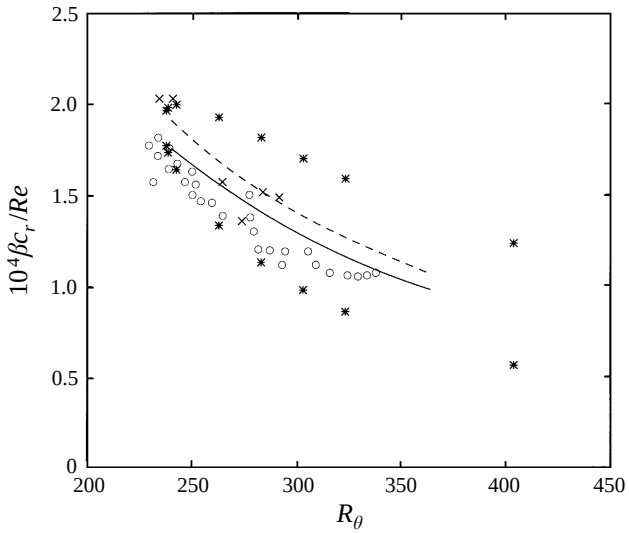


FIGURE 17. Nonlinear maximum amplification rate curve (solid) in $R_\theta$ scaled frequency $10^4\beta c_r/Re$ space. Superimposed its linear eigenvalue problem or initial-boundary-value problem counterpart (dashed). Experimental results of Pfenninger and Bacon (1969) are denoted by symbol 'o' and those of Poll (1979) are denoted by symbol '×'. Denoted by symbol '⁎' is the EVP neutral loop.

solutions being stable, it was pointed out that the experimentally observed waves also originated at Branch I. The present calculations suggest that at nonlinear levels these waves have a maximum amplification rate curve which lies very close to the experimentally observed waves (cf. figure 17). Such solutions render the LEBL flow analogous to the classical incompressible flat-plate flow in terms of the location, in parameter space, of the experimentally observed waves.

Turning to the question of subcriticality, it is of interest to examine the conjecture of the absence of growing solutions below the linear critical *Re*, either by imposing larger initial disturbances and/or by permitting longer integration times than those currently used (suggested by the linear problem and also used by Hall & Malik, 1986); a solution departing from the linear behaviour, if supported by the system

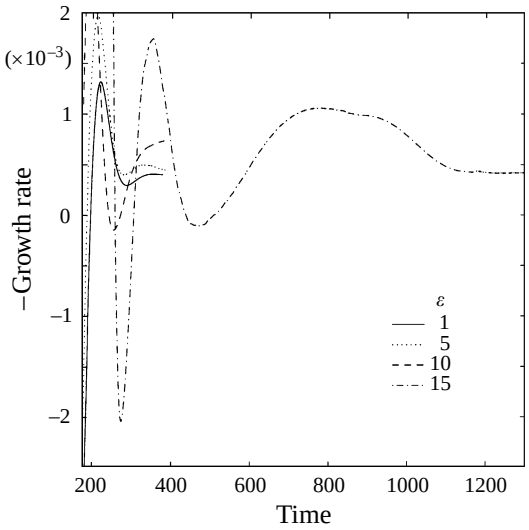


FIGURE 18. Nonlinear growth rates time history for different initial excitation amplitudes.

(2.7)–(2.15), is expected to become increasingly apparent as $\varepsilon$ is increased (also, as time progresses). Results at the subcritical $Re = 550$ were obtained for a succession of initial excitation amplitudes, $\varepsilon = 1, 5, 10$ and 15. The growth rates were plotted against time and, omitting the early transient behaviour for clarity, are presented in figure 18. The effect of an increasing amplitude of the initially imposed excitation $\varepsilon$ is that, in the process of converging, the growth rates of the instability waves present in the flow are positive for increasingly longer times, indicating growth. This behaviour is absent in the linear result; in the linear case a converged result corresponding to a decaying wave is quickly obtained. However, it may be seen in figure 18 that even the highest $\varepsilon$ calculation performed eventually produces results that fall back to growth rates of the sign predicted by linear theory. This linear result may be inferred on this curve by the converged value of the $\varepsilon = 1$ calculation. Figure 19 is a plot of growth rates against wavenumber and it may be seen that both the maximally and all less-amplified modes at $Re = 550$, $\varepsilon = 15$ are, in fact, all damped. It is interesting to compare these nonlinear results to the linear predictions of table 3. The result of main importance with respect to subcritically growing solutions is the level of the maximum value of the damping rate. It may be seen in figure 19 that the value delivered by the nonlinear calculation is $\omega_i \approx -4.1 \times 10^{-4}$ as opposed to a value of $\omega_i \approx -3.9 \times 10^{-4}$ yielded by the linear version of the code. Not only does the nonlinear solution at these parameters correspond to damping waves but it turns out that these waves are more stable than their linear counterparts.

The nonlinear curve in figure 19 has departed from the linear result in the manner qualitatively predicted in figures 14 and 16. A quantitative difference that exists between the results of figures 14 and 19 is worthy of discussion.† Decaying waves predicted by a nonlinear calculation at a given point in $(\beta, \omega_i)$ parameter space may in time fall to linear levels; provided there is sufficient integration time for the nonlinear solution, the linear and nonlinear dependencies of growth rates on wavenumber

† Thanks are due to a Referee for pointing out this subtle and important point.

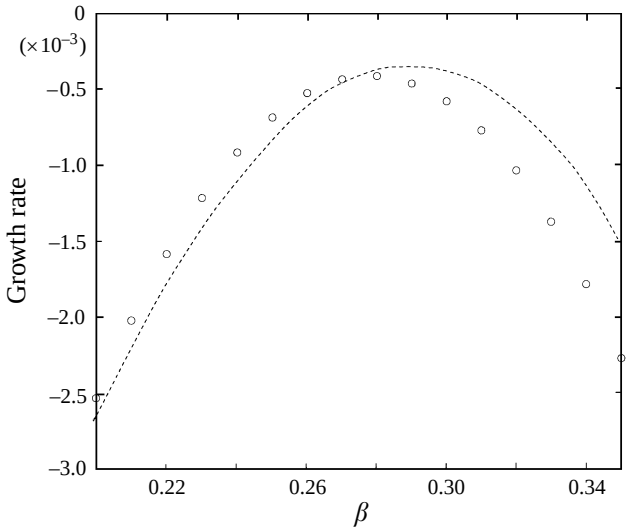


FIGURE 19. Growth rates obtained by nonlinear (symbols) and linear (dashed) solution of (2.7)–(2.12) against wavenumber at the subcritical $Re = 550$.

will eventually agree at this point. In this respect further integration in time of the nonlinear flow-field for $Re = 800$, presented in figure 14, may result in a neutral loop which is wider than the respective linear loop at this linearly unstable Reynolds number. By contrast, the nonlinear calculation presented in figure 19 already delivers a branch I which largely agrees with the respective linear result and the only further possibility for the nonlinearly decaying solution in the neighbourhood of branch II is to fall back to the linear result. This scenario would certainly hold true had we introduced disturbances at small amplitudes into the nonlinear code and integrated in time until disturbances reached nonlinear levels. When we followed such an approach the discrepancy between the linear and nonlinear neutral loops obtained was negligible (cf. figures 9, 10 and 22). In the runs where a large value of $\varepsilon$ was used to introduce nonlinear disturbances from the beginning of the calculation, on the other hand, it is unclear how the nonlinear results relate to those obtained using a low $\varepsilon$ value; it may be that the nonlinear solution has already been attracted away from its linear counterpart from the early stages of the calculation.

The central question addressed, however, namely whether nonlinear subcritically growing solutions exist, can be answered by reference to the maximum value of $\omega_i$ obtained from its dependence on $\beta$. This is at the levels predicted by the linear result, irrespective of the $\varepsilon$ value utilized. Consistently with the solutions to the present two-dimensional problem obtained by Jiménez *et al.* (1990) and unlike the numerical results in the work of Hall & Malik (1986), no two-dimensional subcritical states have been found. In this light, the observation of subcritical turbulence in the DNS of Spalart (1988) and the analogous result of Corral & Jiménez (1994) must be interpreted as a consequence of the three-dimensionality permitted in their DNS codes. A viscous mechanism analogous to the inviscid one suggested by Hall & Seddougui (1990) might be examined with respect to the breakdown of potentially existing nonlinear equilibria to turbulent flow in the attachment-line boundary layer. Such a conjecture, of course, requires theoretical foundation and, at the very least, numerical verification that no DNS to date has provided.

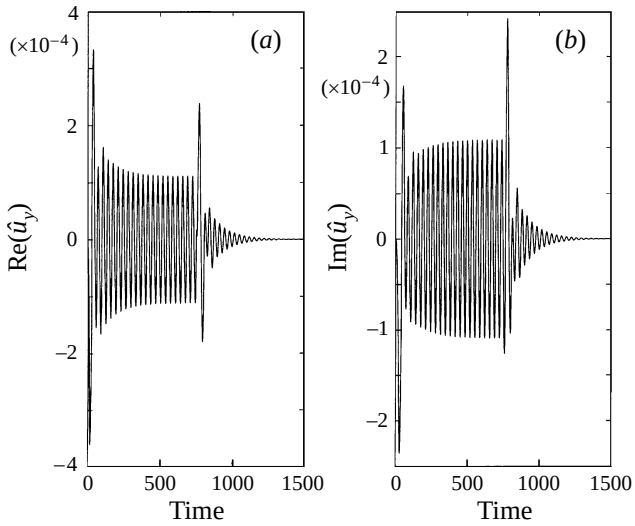


FIGURE 20. Wall shear vs. time under a succession of wall forcing functions at $Re = 550$. The ribbon-like forcing initially creates a neutral wave of the imposed frequency; after it is being removed at $t = 750$ a decaying wave emerges.

### 3.2. *A model for the vibrating ribbon*

We now present a final attempt to investigate the possibility of nonlinear interactions causing the flow to depart from the behaviour predicted by linear theory. While modelling the vibrating ribbon technique, used in experiments, requires (three-dimensional) spatial simulations, we obtain here solutions subject to the form of forcing

$$F(t) = \sin(\omega_r(\beta)\ t)\,. \tag{3.6}$$

In this manner, each wavenumber $\beta$ may be excited individually, with an arbitrarily chosen frequency $\omega_r$. Here we choose to force each mode by its corresponding linear least-stable frequency. This may be achieved in a number of ways. The initial-boundary-value problem approach may be utilized in order to obtain the function $\mathrm{Re}\{\omega\} \equiv \omega_r(\beta)$, after transients of the solution have subsided; such an approach is attractive since the converged results of the scheme in question contain the functional dependence of frequency and growth rates on the spanwise wavenumber at a given Reynolds number. Alternatively, we utilize results of the solution to the eigenvalue problem presented in §2.3.

At $Re = 550$, in view of the strongly damped nature of the linear modes outside this range, we focus on $\beta \in [0.15, 0.45]$, setting $F(t)$ outside this range identically equal to zero, which amounts to exciting only the least-stable linear modes. We first ensure that no numerical artifacts are introduced by the alteration of the forcing function. To this end, (nonlinear) numerical solutions are obtained under a succession of the forcing functions (3.6) and (3.5); the result is presented in figure 20. At this set of parameters a neutral wave is seen to be established and sustained for as long as the forcing (3.6) is maintained. The ribbon-like forcing (3.6) is then removed and two courses of action are taken. The flow is permitted to settle without any further forcing, or the forcing (3.5) is reinstalled. Despite repetition at a number of initial amplitudes $\varepsilon = 0.01$, 0.1, and 1, we observed that the forcing (3.6) always resulted in neutral solutions and, subsequently, the growth rate results predicted by (3.5) (and

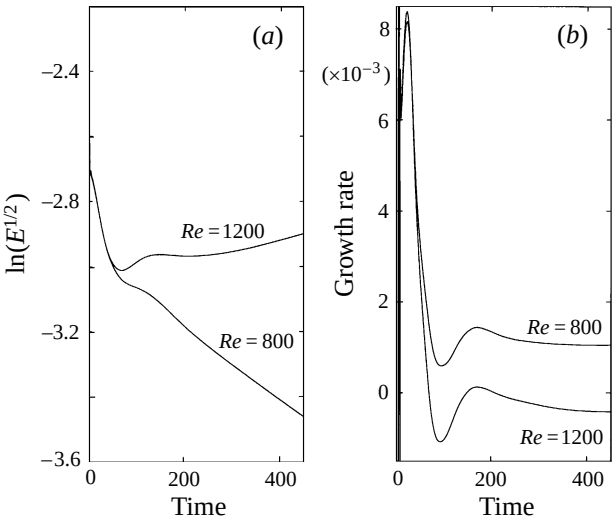


FIGURE 21. Nonlinear behaviour of mode $\beta = 0.3$ at suction $\kappa = -0.1$; (*a*) perturbation energy evolution with time; (*b*) corresponding growth rate.

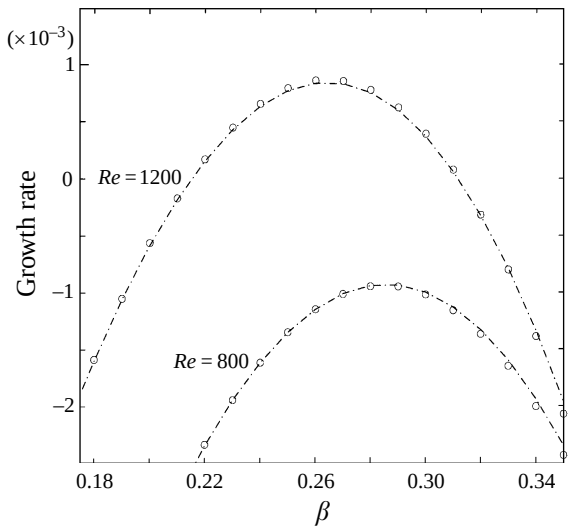


FIGURE 22. Nonlinear against Linear dependence of growth rate on wavenumber at $Re = 800$ and $Re = 1200$. Dashed: linear; Symbols: nonlinear.

approximated by linear theory) were eventually obtained, namely decaying waves. Under no conditions were we able to reproduce numerically the solutions reported by Hall & Malik (1986).

### 3.3. *The effect of suction*

A final question raised by weakly nonlinear theory is whether suction is an effective means of control of instability. Although it increases the critical Reynolds number, suction makes the flow more susceptible to subcritical disturbances (Hall & Malik 1986). Countering this theoretical argument the three-dimensional nonlinear computations of Spalart (1988) demonstrated that suction is an effective method of

stabilizing disturbances. We address this question in the framework of the present nonlinear initial-boundary-value problem formulation.

Simulations were performed at $\kappa = -0.1$, and two values of Reynolds number $Re = 800$ and $Re = 1200$ which correspond, respectively, to linearly stable and linearly unstable conditions; we present the results in figures 21 and 22. In figure 21($a$) the time evolution of the perturbation energy at $\beta = 0.3$ is presented for both Reynolds numbers. By the end of the time integration the flow is seen to have settled, at least qualitatively, to the behaviour predicted by linear theory; in figure 21($b$) the respective growth rates confirm this assertion. In figure 22 the growth rate dependence on wavenumber is presented, as obtained at the end of both simulations. Superimposed is the linear result obtained by the linearized version of the code. Higher $\varepsilon$ values were not considered in this context but, at least up to the time considered, the nonlinear response of the flow to suction in the parameter range considered is seen to be identical to that which linear theory predicts.

## 4. Discussion

To date there exists no experimental information on growth rates or spatial structure of eigenfunctions pertinent to linear instability in the swept attachment-line boundary layer. It may, therefore, appear questionable whether nonlinear theoretical studies on the basis of the Görtler–Hämmerlin assumption on linear disturbances should be pursued. A comprehensive comparison of the possible two-dimensional linear approaches is presented, however, which further establishes the ability of the GH linear model to deliver information on the linear disturbances in two ways. First, we demonstrate that the eigenvalue problem and initial-boundary-value problem formulations deliver identical results, the latter at the limit of small perturbations and having the obvious advantage of permitting nonlinear studies. Second, we show that the range of frequencies of unstable waves measured in recent experiments corresponds to the neighbourhood of maximally amplified linear GH disturbances. Nonlinear equilibria established on the basis of GH disturbances may, therefore, be considered as relevant theoretical models for the description of flow behaviour.

Contradictory evidence exists in the literature regarding the role of nonlinear subcritical disturbances arising from linear GH perturbations. We have addressed this issue from the point of view of numerical solution to the initial-boundary-value problem problem, utilizing general forms of input disturbances at varying amplitudes to excite the flow. We adhered to the GH assumption in order to be able to, firstly, directly compare our results with the relevant investigations and, secondly, draw conclusions purely on the role of nonlinearity. At low amplitudes of the imposed initial disturbance, instability waves are seen to emerge in our simulations that compare well with those predicted by the eigenvalue problem approach. At supercritical conditions, as the size of the input disturbance is increased, nonlinear solutions have been obtained that bifurcate from the linear loop in the manner predicted by earlier analysis and observed in simulations. The nonlinear loops obtained are all confined in a thin region around the linear loop; a consequence of the departure of the nonlinear neutral loops from their linear counterpart is that the maximum amplification rate of the nonlinear neutral curve lies very close, in parameter space, to the experimentally observed waves, a behaviour analogous to that observed experimentally in Blasius flow.

At the subcritical Reynolds number $Re = 550$ extensive numerical experimentation has been performed in order for growing solutions to be identified and conditions for

equilibrium to be established. General disturbances were introduced at increasingly higher amplitudes into the flow; despite large integration times the growth rates of the instability waves established at this Reynolds number correspond to decaying perturbations. Combined with the nonlinear maximum amplification rate dependence on *Re*, obtained herein, this result suggests the absence of subcritical instability of the nonlinear two-dimensional model LEBL flow. This prediction is in line with the analogous result of Jiménez *et al.* (1990) and in contrast to earlier numerical solutions of the same model problem. The reported existence of subcritical nonlinear equilibria in the work of Joslin (1995) may be reconciled with the present results on the grounds of the three-dimensionality of Joslin's code. Indeed, three-dimensionality has permitted (subcritical) breakdown to turbulence in the earlier DNS of both Spalart (1988) and Corral & Jiménez (1994).

The present contribution has demonstrated that the framework of Görtler–Hämmerlin disturbances is too narrow for subcriticality of the LEBL flow to be reproduced. Inclusion of three-dimensionality should be the essential departure point for any future theoretical model that aims to explain subcritical instability and turbulence in the swept attachment-line boundary layer.

The present work commenced while the author was at the University of Twente, the Netherlands. An Alexander von Humboldt research fellowship enabled its completion at DLR Göttingen. The able advice provided by Dr P. W. Duck during the early stages of the present work is gratefully acknowledged. Discussions with Professors D. I. A. Poll and J. Jiménez are kindly appreciated. Computations were performed on the Amdahl VP1200 at the Manchester Computing Centre, on the Cray Y-MP4/464 at Stichting Academisch Rekencentrum Amsterdam under NCF grant 93.0138, and on the NEC-SX3 at DLR Göttingen.

## Appendix A. Collocation solution of the temporal eigenvalue problem

The discrete form of (2.16)–(2.17) may be obtained by appropriately specifying a mapping transformation for the independent variable $\eta \in [0, \infty)$ onto the standard Chebyshev domain $x \in [-1, 1]$. We solved (2.16)–(2.17) using up to 100 collocation points redistributing the standard Chebyshev Gauss–Lobatto points $x_j$ on to the calculation grid $\eta_j$ according to

$$\eta_j = l\frac{1 - x_j}{1 + s + x_j} \tag{A 1}$$

with $l$ a length scale and $s = 2l/\eta_\infty$. The location where the calculation domain for the basic flow is truncated is denoted by $\eta_\infty$. Incorporating the metrics of the transformation into the Chebyshev collocation derivative matrices (Boyd 1989),

$$D^{(1)}_{k,j} = \begin{cases} \frac{1}{6}(2N^2 + 1), & j = k = 0 \\ -\dfrac{x_j}{2(1 - x_j^2)}, & j = k \\ \dfrac{\bar{c}_k}{\bar{c}_j}\dfrac{(-1)^{j+k}}{x_k - x_j}, & j \neq k \\ -\frac{1}{6}(2N^2 + 1), & j = k = N \end{cases}$$

with

$$\overline{c}_j = \begin{cases} 2, & j = 0 \\ 1, & 1 \leqslant j \leqslant N-1 \\ 2, & j = N \end{cases}$$

we write (2.16)–(2.17) as a generalized eigenvalue problem

$$\mathscr{A}\phi = c\mathscr{B}\phi. \tag{A 2}$$

Denoting the Chebyshev collocation derivative matrix, modified by incorporation of the metrics, by $\widehat{D}$, the entry $a_{i,j}$ of $\mathscr{A}$, for example, is given by

$$a_{i,j} = \begin{cases} \left(\widehat{D}^2_{i,j} - \overline{v}_i\widehat{D}_{i,j} - \beta^2 - 2\overline{u}_i - \mathrm{i}\beta Re\overline{w}_i\right)\hat{u} - (\widehat{D}_{i,j}\overline{u}_i)\hat{v}, & i = j;\ i = j = 0, n \\ \left(\widehat{D}^2_{i,j} - \overline{v}_i\widehat{D}_{i,j}\right)\hat{u}, & i \neq j;\ i = j = 0, n \end{cases}$$

as dictated by the minimization of the residuals. Six rows of both arrays $\mathscr{A}$ and $\mathscr{B}$ have to be reserved for the imposition of the boundary conditions associated with the problem.

## Appendix B. Extraction of frequency and growth rate information from DNS data

We employed three different methods for the numerical calculation of the frequency and the growth rates. These exploit both physical information of the solution sought as well as technical properties of the algorithm developed. Past the early transient state the solution settles to that predicted by linear stability theory (cf. figure 7). During linear growth/decay a (complex) Fourier component of *any* flow quantity $\hat{q}^*(\beta, y, t)$ takes the form $\hat{q}^*(\beta, y, t) = \tilde{q}^*(y)\exp\{\mathrm{i}(\beta z - \omega t)\}$. Owing to the linear behaviour of the solution in this regime, individual wavenumber $\beta$ values may be monitored in isolation from all other wavenumbers, and the solution at a given $\beta$ may be written as $\hat{q}^*_b(y, t) = \tilde{q}^*(y)\exp\{\mathrm{i}\omega t\}$. Frequency and growth rate information may then be calculated by any of the following methods.

*Method 1:* $\omega = (1/\hat{q}^*_b)\,\mathrm{d}\hat{q}^*_b/\mathrm{d}t$.
The Fourier components $\hat{q}^*_b$ of any flow quantity for which we solve are available at all times and, subject to availability of the derivative $\mathrm{d}\hat{q}^*_b/\mathrm{d}t$, the frequency and the growth rates of the instability wave are, respectively, $\mathrm{Re}\{\omega\}$ and $\mathrm{Im}\{\omega\}$.

*Method 2:* $\omega = \{\ln\hat{q}^*_b(t + \Delta t) - \ln\hat{q}^*_b(t)\}/(\mathrm{i}\Delta t)$.
The necessary elements here are the Fourier components of the solution at two successive times $t$ and $t + \Delta t$.

*Method 3:* $\mathrm{Im}\{\omega\} = \mathrm{d}F_b(t)/\mathrm{d}t$
where $F_b(t) = \ln(E_b(t))^{1/2}$ and $E_b(t) = \displaystyle\int_{y=0}^{y_\infty}\{\hat{u}^2 + \hat{v}^2 + \hat{w}^2\}\,\mathrm{d}y$.

When using methods 1 and 2 one may arbitrarily choose to monitor the value of *any* component of the solution $\hat{q}^*_b$ at *any* location $y$ along the entire domain in the wall-normal direction, or take $\hat{q}^*_b$ to be a physical quantity which may be constructed using information at a fixed $\beta$ location and time (e.g. wall shear). Method 3, on the other hand, incorporates information from all $y$-locations.

The numerical calculation of the time derivatives which appear in methods 1 and 3 takes advantage of the fact that a constant time step is utilized in the implicit

| $m$ | $C_{m,n-5}$ | $C_{m,n-4}$ | $C_{m,n-3}$ | $C_{m,n-2}$ | $C_{m,n-1}$ | $C_{m,n}$ |
|---|---|---|---|---|---|---|
| 2 | | | | −1 | 4 | −3 |
| 3 | | | 2 | −9 | 18 | −11 |
| 4 | | −6 | 32 | −72 | 96 | −50 |
| 5 | 240 | −150 | 400 | −600 | 600 | −274 |

TABLE 4. Coefficients for numerical calculation of first derivative with second-to-fifth-order accuracy using backward differences on a uniform grid.

| | $m$ | $\omega_r \times 10$ | $\omega_i \times 10^3$ |
|---|---|---|---|
| Method 1 | 2 | 1.2547832 | 2.5084320 |
| | 3 | 1.2543749 | 2.5039661 |
| | 4 | 1.2543736 | 2.5049228 |
| | 5 | 1.2543738 | 2.5049271 |
| Method 2 | | 1.2543738 | 2.5049262 |
| Method 3 | 2 | | 2.5049265 |
| | 3 | | 2.5049265 |
| | 4 | | 2.5049265 |
| | 5 | | 2.5049265 |

TABLE 5. Frequency and growth rates obtained in DNS by the three methods at $\kappa = 0.18$, $Re = 350$, $\beta = 0.3053125$ and $Ny = 251$.

scheme for time integration to evaluate derivatives $f'$ at time level $n$ of a function $f$ whose values are known at times $n, \ldots, n-m$ using the $m$th-order-accurate one-sided (backward) schemes (e.g. Abramowitz & Stegun 1970)

$$f'_n = \frac{1}{m!(\Delta t)} \sum_{i=n-m}^{n} C_{m,i} f_i; \quad m = 2, \ldots, 5,$$

with the coefficients of the differentiation presented in table 4.

Results of application of these schemes to the calculation of the time derivatives appearing in methods 1 and 3 are presented in table 5. It is clear that only method 1 is affected by the order of accuracy of the scheme used. A second-order-accurate scheme used in this method delivers the first four digits of the converged result while at least a fourth-order-accurate scheme is necessary to extract the converged result from the DNS data. The result delivered by methods 2 and 3, on the other hand, is the value to which method 1 converges; it is unaffected by the order of accuracy of differentiation in method 3. This difference in behaviour between methods 1 and 3 may be attributed to the fact that the former does not assume any particular form for the behaviour of the solution, in contrast to the latter which implicitly incorporates the exponential behaviour of the DNS solution in the linear regime. For the same reason method 2 also is capable of delivering the converged frequency and growth rate information using a simple algebraic operation on the DNS data. Based on these considerations we have used method 2 to evaluate $\omega$ at the linear regime and method 3 to cross-validate the results presented.

Incidentally, we note that methods 2 and 3 are also straightforwardly applicable to an algorithm which uses explicit time integration since they are capable of delivering results using information from two successive time levels alone; consequently methods 2 and 3 are unaffected by a possibly variable time step that the CFL condition imposes in explicit time-integration schemes.

## REFERENCES


Abramowitz, M. & Stegun, I. A. 1970 *Handbook of Mathematical Functions*. Dover.

Adams, N. A. 1993 Numerische Simulation von Transitionsmechanismesn in kompressiblen Grenzschichten. *DLR-FB* 93-29.

Arnal, D. 1993 Boundary layer transition: Predictions based on linear theory. *AGARD Rep.* 793, pp. 2-1–2-63.

Arnal, D., Coustols, E. & Jullien J. C. 1984 Etude expérimentale et théorique de la transition sur une aile en fléche infinie. *La Recherche Aérospatiale* **4**, 275–290.

Bertolotti, F. P. 1991 Linear and nonlinear stability of boundary layers with streamwise varying properties. Ph.D Thesis, The Ohio State University, Columbus, Ohio.

Boyd, J. P. 1989 *Chebyshev and Fourier Spectral Methods*. Lecture Notes in Engineering, vol. 49. Springer.

Canuto, C., Hussaini, M. Y., Quarteroni, A. & Zang, T. A. 1988 *Spectral Methods in Fluid Dynamics*. Springer.

Corral, R. & Jiménez, J. 1994 Direct numerical determination of the minimum bypass Reynolds number in boundary layers. In *Applications of Direct and Large Eddy Simulation to Transition and Turbulence. AGARD CP*-551, pp. 19-1–19-10.

Duck, P. W. & Burggraf, O. R. 1986 Spectral solutions for three-dimensional triple-deck flow over surface topography. *J. Fluid Mech.* **162**, 1–22.

Floryan, J. M. & Dallmann, U. 1990 Flow over a leading edge with distributed roughness *J. Fluid Mech.* **216**, 629–656.

Gaster, M. 1962 A note on the relation between temporally increasing and spatially increasing disturbances in hydrodynamic stability. *J. Fluid Mech.* **14**, 222–224.

Gaster, M. 1965 A simple device for preventing turbulent contamination on swept leading edges. *J. R. Aero Soc.* **69**, 788–789.

Gaster, M. 1967 On the flow along swept leading edges. *Aero. Q.* **18**, 165–184.

Goldstein, S. (ed.) 1938 *Modern Developments in Fluid Dynamics*. Oxford University Press.

Görtler, H. 1955 Dreidimensionale Instabilität der ebenen Staupunktströmung gegenüber wirbelartigen Störungen. In *50 Jahre Grenzschichtforschung* (ed. H. Görtler & W. Tollmien) pp. 304–314. Vieweg und Sohn.

Gray, W. E. 1952 The effect of wing sweep on laminar flow. *RAE TM Aero* 255.

Gregory, N., Stuart, J. T. & Walker, W. S. 1955 On the stability of three-dimensional boundary layers with application to the flow due to a rotating disc. *Phil. Trans. R. Soc. Lond.* A **248**, 155–199.

Grosch, C. E. & Salwen, H. 1978 The continuous spectrum of the Orr-Sommerfeld equation. Part 1. The spectrum and the eigenfunctions. *J. Fluid Mech.* **87**, 33–54.

Hall, P. & Malik, M. R. 1986 On the instability of a three-dimensional attachment-line boundary layer: weakly nonlinear theory and a numerical approach. *J. Fluid Mech.* **163**, 257–282.

Hall, P., Malik, M. R. & Poll, D. I. A. 1984 On the stability of an infinite swept attachment-line boundary layer. *Proc. R. Soc. Lond.* A **395**, 229–245.

Hall, P. & Seddougui, S. O. 1990 Wave interactions in a three-dimensional attachment-line boundary layer. *J. Fluid Mech.* **217**, 367–390.

Hämmerlin, G. 1955 Zur instabilitätstheorie der ebenen Staupunktströmung. In *50 Jahre Grenzschichtforschung* (ed. H. Görtler & W. Tollmien), pp. 315–327. Vieweg und Sohn.

Herbert, T. 1977 Die neutrale Fläche der ebenen Poiseuille Strömung. Habilitation, Universität Stuttgart.

Hiemenz, K. 1911 Die Grenzschicht an einem in den gliechförmigen Flüssigkeitsstrom eingetauchten geraden Kreiszylinder. Thesis, Göttingen. Also *Dingl. Polytechn. J.* **326**, 321–324.

Horten, R. & Selinger, P. F. 1983 *Nurflügel - Die Geschichte der Horten-Flugzeuge 1933–1960*. H. Weishaupt.

Jiménez, J., Martel, C., Agüí, J. C. & Zufiria, J. A. 1990 Direct numerical simulation of transition in the incompressible leading edge boundary layer. *Tech. Note ETSIA* MF-903.

Joslin, R. D. 1995 Direct simulation of evolution and control of three-dimensional instabilities in attachment-line boundary layers. *J. Fluid Mech.* **291**, 369–392.

Koch, W. 1992 On a degeneracy of temporal secondary instability modes in Blasius boundary-layer flow. *J. Fluid Mech.* **243**, 319–351.

Laurien, E. & Kleiser, L. 1989 Numerical simulation of boundary layer transition and control. *J. Fluid Mech.* **199**, 403–440.

Lippisch, A. 1976 *Ein Dreieck fliegt: Die Entwicklung der Delta-Flugzeuge bis 1945*. Motorbuch Verlag, Stuttgart.

Macaraeg, M. G., Streett, C. L. & Hussaini, M. Y. 1988 A spectral collocation solution to the compressible stability eigenvalue problem. *NASA* TP-2858.

Morkovin, M. V. & Reshotko, E. 1989 Dialog on progress and issues in stability and transition research. In *IUTAM Symposium on Laminar-Turbulent Transition* (ed. D. Arnal & R. Michel), pp. 3–29. Springer.

Numerical Algorithms Group 1992 Scientific Library. Mark 15.

Orszag, S. A. 1971 Accurate solution of the Orr-Sommerfeld stability equation. *J. Fluid Mech.* **50**, 689–703.

Pfenninger, W. & Bacon, J. W. 1969 Amplified laminar boundary layer oscillations and transition at the front attachment line of a 45° swept flat-nosed wing with and without suction. In *Viscous Drag Reduction* (ed. C. S. Wells), pp. 85–105. Plenum Press.

Poll, D. I. A. 1979 Transition in the infinite swept attachment line boundary layer. *Aero. Q.* **30**, 607–629.

Poll, D. I. A. 1985 Some observations of the transition process on the windward face of a long yawed cylinder. *J. Fluid Mech.* **150**, 329–356.

Poll, D. I. A., Danks, M. & Yardley, M. R. 1996 The effects of suction and blowing on stability and transition at a swept attachment line. In *Transitional Boundary Layers in Aeronautics* (ed. R. A. W. M. Henkes & J. L. van Ingen). Elsevier.

Pruett, C. D., & Streett, C. L. 1991 A spectral collocation method for compressible, non-similar boundary layers. *Intl J. Numer. Meth. Fluids* **13**, 713–737.

Reed, H. L. & Saric, W. S. 1989 Stability of three-dimensional boundary layers. *Ann. Rev. Fluid Mech.* **21**, 235–284.

Reed, H. L. Saric, W. S. & Arnal, D. 1996 Linear stability theory applied to boundary layers. *Ann. Rev. Fluid Mech.* **28**, 389–428.

Rosenhead, L. 1963 *Laminar Boundary Layers*. Oxford University Press.

Spalart, P. R. 1988 Direct numerical study of leading-edge contamination. *AGARD CP*-438, pp. 5-1–5-13.

Streett, C. L., Zang, T. A. & Hussaini, M. Y. 1984 Spectral methods for solution of the boundary layer equations. *AIAA Paper* 84-0170.

Stuart, J. T. 1960 On the non-linear mechanics of wave disturbances in stable and unstable parallel flows. Part 1. The basic behaviour in plane Poiseuille flow. *J. Fluid Mech.* **9**, 353–370.

Theofilis, V. 1993 Numerical experiments on the stability of leading edge boundary layer flow: A two-dimensional study. *Intl J. Numer. Meth. Fluids* **16**, 153–170.

Theofilis, V. 1995 Spatial stability of incompressible attachment-line flow. *Theor. Comput. Fluid Dyn.* **7**, 159–171.

Theofilis, V., Duck, P. W. & Poll, D. I. A. 1989 An investigation of nonlinear instability of flow near a swept attachment line. In *IUTAM Symposium on Laminar-Turbulent Transition* (ed. D. Arnal & R. Michel), pp. 389–394. Springer.

Watson, J. 1960 On the non-linear mechanics of wave disturbances in parallel flows. Part 2. The development of a solution for plane Poiseuille and for plane Couette flow. *J. Fluid Mech.* **9**, 371–389.

Wilkinson, J. H. 1965 *The Algebraic Eigenvalue Problem*. Clarendon.

Wilson, S. D. R. & Gladwell, I. 1978 The stability of a two-dimensional stagnation flow to three-dimensional disturbances. *J. Fluid Mech.* **84**, 517–527.